In the name of God

Communications in Catalysis (Abbreviation: CIC) is an international, open access, online/printed scholarly biannual publication issued by the Department of Chemistry, Azarbaijan Shahid Madani University, Tabriz, Iran. High quality original papers in English dealing with experimental, theoretical and applied research related to catalysis science and technology are welcomed by CIC. This journal provides a forum for publication of original research papers, short communications, and critical reviews in all branches of chemical science and technology, on catalysts and their application in several areas, such as: organic, inorganic, bioorganic, analytical, polymer, etc. Publication process of the manuscripts submitted to CIC is free of charge. All the submitted manuscripts are peer-reviewed by the editorial board and reviewers of the CIC before acceptance for publication. To submit a new manuscript, please start by reading the journal instructions for authors (http: cic.azaruniv.ac.ir).

Content

Communications In Catalysis
Vol. 1, No. 2, 2024, pp.3-14
DOI: 10.22049/CIC.2018.26191.1019

Azarbaijan Shahid Madani University

The Effect of Pt Thin Films on Efficiency of the Carbon-Based Catalysts for Proton-Exchange Membrane Fuel Cells

Shahab Khameneh Asl[a*], Saeed Behjat[a]

[a]Materials Eng. Department, Mechanical Eng. Faculty, University of Tabriz, Tabriz, IRAN, P.O. Box 5166614766

Corresponding Author. E-mail: address:shah.kh.asl@gmail.com,
Tel: +9841333922468, Fax: 984133377866.

Received: 2024-08-04, Revised: 2024-08-20, Accepted: 2024-08-31

Abstract

With increasing pollution and decrease in global reservoirs of fossil fuels, a lot of interest has been attracted to fuel cells as efficient and clean energy sources. Polymeric (membrane) fuel cells are special type of fuel cells, which can be built in small dimensions and power. These cells use hydrogen (and oxygen or air) and produce water. In these cells, platinum is used as electrode (and electro catalyst) both in anode and cathode, due to its low overvoltage for both hydrogen and oxygen. To increase the efficiency of these coatings, it is best to produce platinum particles with maximum area and it automatically leads to nanometric particles. In this thesis, platinum particles are electrodeposited first on Floride doped Tin Oxide (FTO) and then on graphite. Electro deposition is conducted via DC and pulse methods. Floride doped Tin Oxide (FTO) samples have been examined using voltametry in 0.5M H_2SO_4 and graphite samples have been examined in 0.5 M H_2SO_4 + 0.5 M CH_3OH. Specific area of platinum on Floride doped Tin Oxide (FTO) substrates has been calculated. In graphite substrates, comparative analysis has been performed. Prepared samples have been examined using scanning electron microscope. For Floride doped Tin Oxide (FTO) sample, AFM test has been performed to approve the results of SEM. According to results, Platinum particles with approximate diameter of 30 nanometers have been successfully coated on Floride doped Tin Oxide (FTO) and graphite.

Keywords: Nanometric coating, Pulse Electro deposition, Pt/C, Polymeric fuel cells

Introduction

Sir William Grove was the first to build a real fuel cell in 1839 after succeeding in constructing a larger battery (Pew Groove) in 1838. Fuel cells are less polluting than traditional heavy-duty batteries with toxic materials and hazardous nuclear technology. Unlike internal combustion engines that burn fossil fuels and produce toxic gases, the use of fuel cells is the only final product of water vapor [2]. Fuel cells are divided according to the type of electrolyte and type of electrode. Typically, this category includes four major groups. Solid oxide cells, alkaline molten salt cells, sulfuric acid powders and polymer powders. Polymer cells work at ambient temperature and use conductive polymers as electrodes. These fuel cells have been created from a solid polymer electrolyte with porous channels to facilitate the transfer of ions. Due to practical problems with the use of liquid electrolytes, porous or penetrating solid membranes are used in PEM fuel cells [2].

The governing equations for these cells are as follows:

(1) anode $2H_2 \xrightarrow{yields} 4H^+ + 4e^-$

(2) cathode

$$O_2 + 4H^+ + 4e^- \xrightarrow{yields} 2H_2O$$

(3) total reaction

$$2H_2 + O_2 \xrightarrow{yields} 2H_2O\ E^0 = 1.23\ V$$

The theoretical potential of the fuel cell reaction shown above is calculated as follows, which is equal to 1.23 V

(4) $$E^0_{theoretical} = -\frac{\Delta G^0}{nF}$$

During the operation of a fuel cell in non-standard conditions, the activity of the reactants and products is not equal to one, therefore, the voltage of the cell should be calculated from the relation Nernst:

(5) $$E_{theoretical} = E^0_{theoretical} + \frac{RT}{nF} ln \left[\frac{(p_{H_2})(p_{O_2})^{1/2}}{p_{H_2O}}\right]$$

$E_{theoretical}$ is Theoretical voltage of the cell in non-standard conditions, $E_{theoretical}^0$ is Theoretical voltage of the cell under standard conditions, P_{H2}, P_{O2}, and P_{H2O} are the partial pressures of hydrogen, oxygen and water, F Faraday's constant (96485 col / mol), n is the number of electrons produced per mol of hydrogen consumed, R is the global gas constant and T is Kelvin's temperature. By increasing the partial pressure (or concentration) of the reactants, the $E_{theoretical}$ column can be increased [3]. In fact, the actual voltage is lower than the theoretical voltage. Because of the low voltage of oxygen and hydrogen on platinum, these drops are minimized for platinum [4]. so, in polymer platinum systems, platinum acts as a catalyst. Platinum covers, however, have many applications in other catalysts, too [5].

The first experiments on platinum electrolyte deposition, conducted more than 150 years ago by Ellington, who in 1837 recorded a patent certificate in his name, was later followed up by the investigator [6]. In general, today's electrolytes, containing platinum, are stable and very complex. An advantage of these complexes is that they exhibit fewer tendencies to hydrolysis in the bath than

simple salts, and thus the electrolytes are more stable [6]. These electrolytes can be divided into two groups, platinum-containing baths in bivalent and quadrupole states, can be further differentiated in each case with regard to the salts used, which are not always the same as those of the metal sources. In this context, a variety of platinum deposition methods from the chloroplatinic acid solution can be referred to as a deposit at the constant potential of the constant potential deposition (CPD). In a CPD, a potential is applied to the cathode in which platinum (or any other metal) can precipitate until Metallic ions close to the surface. Particle growth is controlled by changing the solution concentration, potential, ionic strength, pH or sedimentation time and electrode [5]. In the PED electrochemical pulsed sedimentation method, negative potential is applied in small time intervals and precipitates the metal from a solution containing ion. In Pulse electrodeposition (PED), a continuous pulse repeats with a light pulse that goes off with a silent pulse, but with an opposite load (or a differential potential other than the potential that the metal precipitate). In addition, platinum nanometer coatings have numerous and growing applications in various industries. Platinum coatings have been applied in different ways on different substrates. Zelenovich, Tripkovich and Rafilevich have covered platinum by thermal decomposition on titanium and examined the methanal oxidation [7]. To do this, the titanium surface has been shaken first to improve adhesion and better bonding. In another study, by Ziao, Blanar and Manoharan, the effect of platinum coverage on zirconia in oxygen sensors has been investigated [8]. In a research conducted by Sallikova, electrochemical sedimentation of platinum from a chlorinated molten bath has been investigated [9]. In another interesting study, Lee, Chan and Phillips have studied the growth of two-dimensional and three-dimensional dendrites in platinum nanoparticles of electrical deposition. As previously mentioned in the same section, platinum tends to produce two-dimensional dendrites in the direction of 110 and three in the direction of 100 [9]. However, this issue has been observed in smaller dimensions. In another study, Driff, Walter and Penn, have deposited particles and platinum nano wires using a galvanic displacement on the Highly Ordered Pyrolytic Graphite (HOPG) substrate [10]. In another research by Huang and Tsai, the electroplating of platinum nanoparticles in carbon-naphtha nanocomposites has been investigated. The purpose of this coating was catalytic properties in the oxidation of methanol [11]. In the older work, Zubimindy, Vasquez, Echo, Vara, Triassic, Sallaraza and Arroyo, the early stages of the platinum sedimentation have been investigated on HOPG [12]. In this paper, there are two goals to be considered: an examination of the effective parameters in increasing the efficiency of the catalysts used in the fuel cells by reducing the grain size and optimizing the conditions in such a way that these factors can be controlled. The ultimate goal of this study is to reduce the particle size of the platinum and increase the fuel cell efficiency. To do this, with regard to what was said, it tried to cover the platinum from its ion-containing solution (chloroplatinic acid H_2PtCl_6) by pulse method. To optimize the conditions, a commercially-operated, electrically controlled system was used.

Experimental procedure

Sedimentation was performed on the FTO glass slabs (Pilkington TEC 15 / 3.2 produced by KINTEC) and graphite (SK1, Seraj Industrial Coal).

Chloroplatinic acid solution was used to precipitate the platinum tetrachloride to prepare it. Potassium tetrachloride (Fluka Chemicals, 100% pure, containing 58% platinum), powdered by adding a stoichiometric amount of concentrated chloride (Merck Chemicals, containing 37.5% HCl in 100 g of solution) and deionised water, dissolves 40 mM of chloroplatinic acid as the base solution was prepared. To control pH from concentrated sulfuric acid (Merck Chemicals, 95-97% H_2SO_4 in 100 g of solution). To prepare the samples for coating, the base with deionized water and ethanol was placed in the ultrasonic cleaner.

In order to apply the constant potential coatings, the Princeton Appliediscount Princeton Opportunity R & C Preston potentiostat / galvanostat EG & G model 273A as well as the Autolab Potentiostatic / Galvanostat PGSTAT 302N was used. Four pulsed samples were prepared according to Table 1 (two FTO samples and two graphite samples) assigned to P1 and P2, and GP1 and GP2. These four samples were precipitated from 0.01 M chloroplatinic acid solution. P1 and GP1 samples were prepared at a pulse voltage of ± 1000 mV (saturated calomel electrode:SCE) and samples of P2 and GP2 at a pulse voltage of ± 500 mV (SCE).

In order to investigate FTO samples, cyclic voltammetric test was used. In these tests, the Autolab device PGSTAT 302N was used in the corrosion lab of Sharif University of Technology. To investigate the surface microstructure of the coating, an ordinary scanning electron microscope of the Razi metallurgy research center and a scanning electron microscope of the Electrical Department of the Faculty of Engineering of the University of Tehran using the HITACHI S4160 model were used. For comparison of SEM images, for example, the FTO was used for atomic force microscopy. The atomic force microscope was used by the associate professor, the Nanosurf model of the Mobile S model.

The metal distribution on the surface of the samples was measured by a system designed to measure the isotherm of hydrogen adsorption. After resuscitation of samples using hydrogen atmosphere at 350 °C, the coating was cooled under vacuum conditions and the isotherm was poorly absorbed and the total pressure was measured at 1-40 rounds at room temperature. The difference between poor absorption and total up to zero pressure was achieved. This indicates a strong absorption of hydrogen, which is generally absorbed on the coating surface metals, now assuming a ratio of one to one hydrogen atom and metal (platinum), the amount of metal surface was measured [13].The heat of absorption of catalyst samples was obtained by using a calorimeter attached to a glass compartment of a C-80 tian-Calvet calorimeter vacuum tube equipped with a diaphragm pump turbomolecule. For measuring the pressure with a Varian CeramiCel pressure gauge in a range of 10 to 10, the negative power of four rounds was used.

Table 1. Specifications of samples and their codes

Sample code	Substrate	Type	Test conditions	analysis	Surface (cm^2)
P1	FTO	Pulse precipitation	Cubic pulse ±1000mV (SCE)	FESEM, cyclic voltammetry 0.5 M H_2SO_4	1.2579
P2	FTO	Pulse precipitation	Cubic pulse ±500mV (SCE)	FESEM, cyclic voltammetry 0.5 M H_2SO_4AFM	1.1855
GP1	Graphite	Pulse precipitation	Cubic pulse ±1000mV (SCE)	FESEM, cyclic voltammetry 0.5 M H_2SO_4, 0.5 M CH_3OH	1.6393
GP2	Graphite	Pulse precipitation	Cubic pulse ±500mV (SCE)	FESEM, cyclic voltammetry 0.5 M H_2SO_4, 0.5 M CH_3OH	0.9577

Results and discussions

The potentials are more positive than the equilibrium potential (Nernistis) [14]. This state usually occurs at the level of an atomic layer, and very rarely of two layers, and in the case of hydrogen on platinum, Underpotential deposition (UPD) can be considered as one layer at high approximation. Each atom of platinum on the particle surface (each surface atom) has the ability to absorb a hydrogen atom. The shape, size, and number of peaks observed on the hydrogen absorbed in a CV depend on the crystalline arrangement of the particle platinum [15]. In addition, the intensity and shape of the absorption and discharging peaks of hydrogen depend on the purity of the electrode, the solubility of the impurities and the nature of the electrolyte. However, the voltage and position of the UPD-related couriers, with a very good approximation, are independent of the speed of the scan and the switching voltage [14]. The area below the UPD Chart is a measure of the load exchanged during the absorption of hydrogen. This time, it specifies the number of hydrogen atoms that are absorbed during the process on the surface of platinum atoms. Given that each atom of platinum absorbs only one hydrogen atom, the number of platinum atoms can be obtained at the electrode surface. In the case of samples with a high background signal of hydrogen and comparable to platinum itself, it is not possible to check the level of platinum with hydrogen UPD. The FTO does not actually produce a signal that is problematic, but carbon intensely raises the signal and will probably hide the UPD-related signals from hydrogen. In this case, other methods are used to check the level of platinum. A methanol solution with half a molar sulfuric acid can be used and methanol oxidation on platinum is studied. With these issues in mind, for the qualitative analysis of (Cyclic Voltammetry) CVs obtained for graphite samples, it can be said that the higher the level below the charts of these peaks (at a scanning speed), the greater

the amount of platinum on the surface. Due to the broader and longer methanol oxidation, this peak was used for data analysis [16,17].

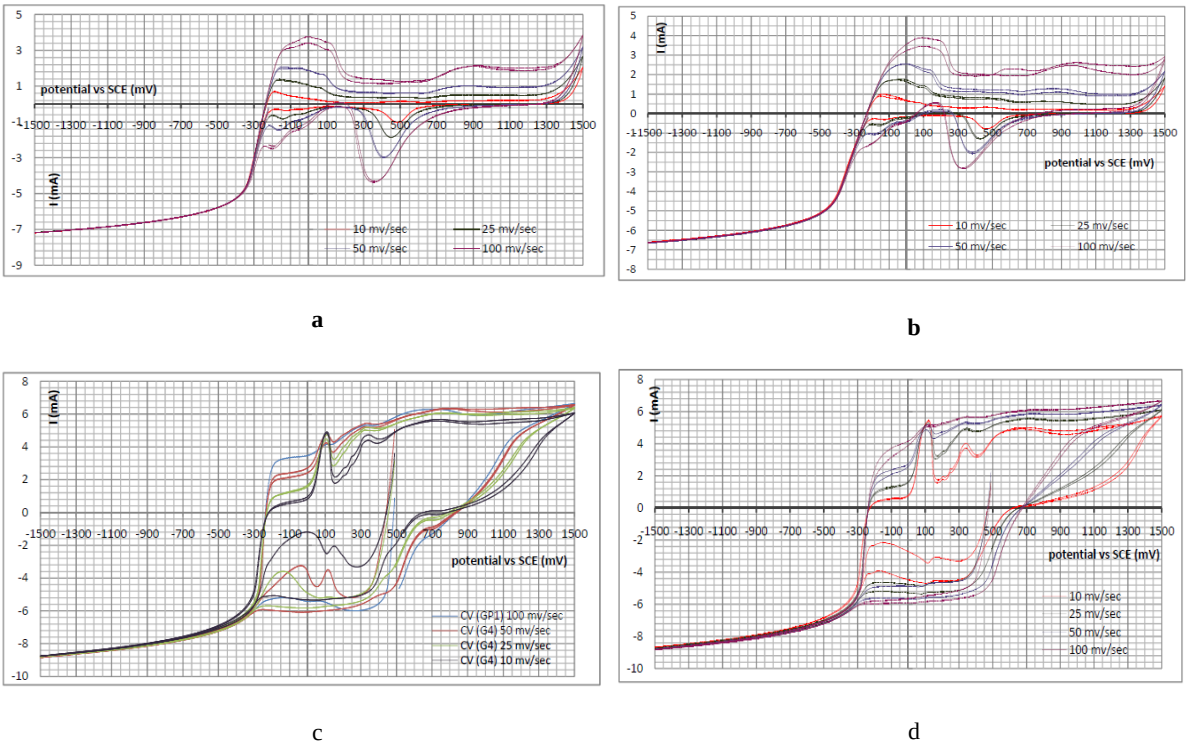

Figure 1. The cyclic voltammetry (CV) of the samples P1 (A) and P2 (B) in a 0.5 M H_2SO_4 solution is two cycles and refers to GP1 (C) GP2 (d) in a solution of + CH_3OH 0.5 M H_2SO_4 0.5 M.

Figure 1 (a) shows the results of the cyclic voltammetric sample P1 (FTO substrate, produced in a pulse of ± 1000 mV (SCE)) in a single cycle at four different scan speeds. The electrode is Ag / AgCl. This test was performed at a reference electrode voltage of SCE = +0.149 mv, the scanning speed was mv / sec 100; the first switch point was 1500 mv (SCE); the second switch point was 1500+ mv (SCE). The surface area of platinum in this sample was calculated as 1.2579 square meters. In Fig. 1b, the results of the cyclic voltammetric of the sample P2 (FTO substrate, produced in a pulse of ± 500 mV (SCE)) in two cycles and at four different scan speeds, respectively, showed a platinum surface area of 1855.1 m^2 Calculated. In the voltammetric studies of graphite specimens, as already mentioned, Hupd's analysis of graphite is not accurate due to the high signal. In this case, methanol oxidation was used. Due to the fact that quantitative analysis by methanol oxidation was not mentioned in the sources, the qualitative analysis of CVs obtained for graphite specimens was determined. In general, it can be said that the higher the level below the charts of these peaks (at a scan speed), the greater the amount of platinum on the surface. Here, too, graphs have been used to show the methane's main courier. Due to the lack of oxygen removal, the resulting charts also have oxygen peaks, which make their analysis a bit more complicated.

Fig. 1C shows the results of the cyclic voltammetric sample GP1 (graphite

substrate, prepared in a pulse of ± 1000 mV (SCE)) in a cycle at four different scan speeds. The platinum level in this sample was 6,393 square meters, which is comparable to that of the FTO. Also in Fig. 1d, the cyclic voltammetric results show the GP2 sample (graphite substrate (SCE)) in a four-speed scan. The platinum level of this sample was 9.577 m^2, which has a noticeable drop in comparison with other samples.

SEM images were prepared from the surface of prepared samples for microstructure analysis of coated samples. Figure 2 (a) to (b) related to the sample P1. In this sample, a portion of the coating was dug during the deposition (it was torn off from the surface), however, until the end of the desired cycles, the test was performed. This image (2) is related to that area. In the area covered, the effects of platinum remained that had branches in the branch. The darker background is the FTO. The magnification of this image is 800 times, after the growth of the platinum layer was grown in layered regions where the platinum structure in that area, as it is seen, was a branch of the branch. This dendrite growth state, as previously mentioned, is common in platinum [9,18,19]. But so far, no pulsed precipitation has been reported.

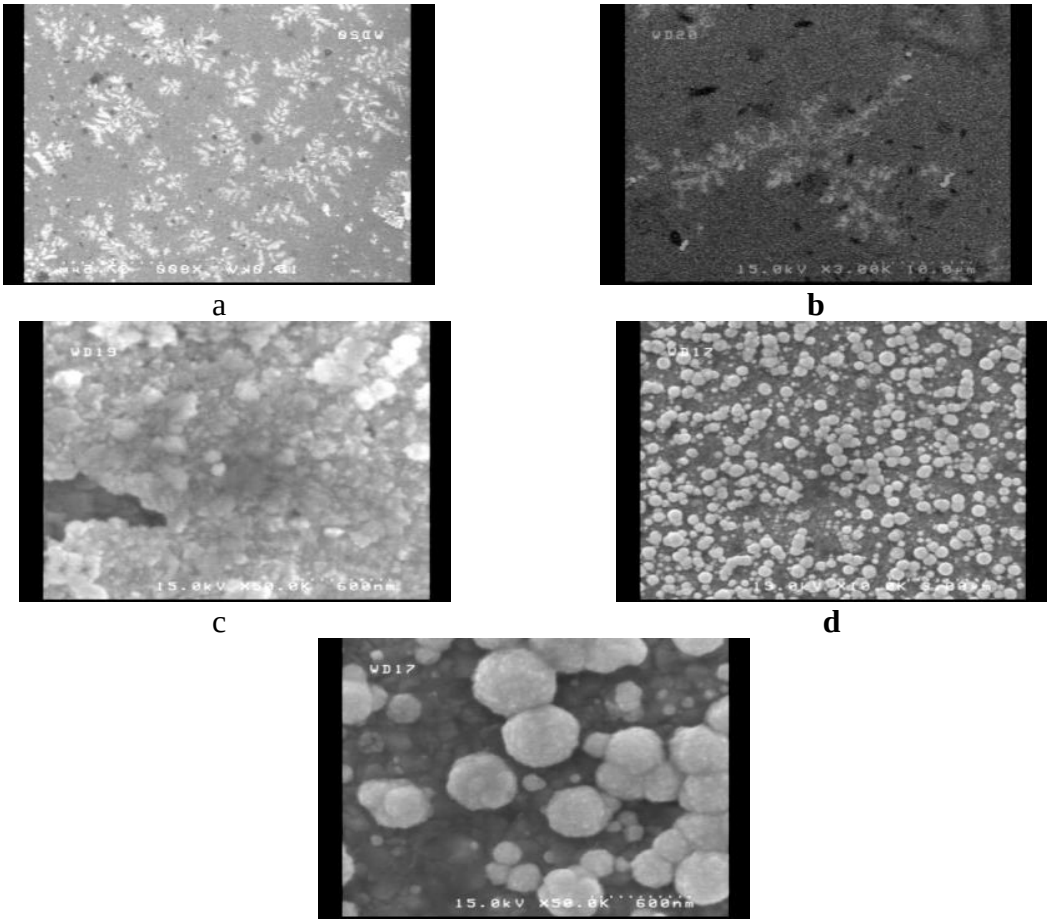

Figure 2. Image of Field Emmition Scanning Electron Microscopy (FESEM) from sample P1. Zoom 800 times (A), 3000 x (B), 50000 x (C), from sample P2. Magnification 15000 x (d), 50,000 x (e).

In Figure 2B, one of these branches is larger and is magnified 3,000 times, which is evident in the development of dendritic form. At this stage, growth is two-dimensional. In Fig. 2C, the sample surface in an apparently unplanned area shows a magnification of 50,000 times. The platinum layer has been completed and agglomerated on a platinum complete layer. However, a hole in this area can be seen without difficulty showing the surface of the FTO. The fine white particles are platinum, which is about 20 nm in size, and the dark field is FTO. The darkness in the middle of the image is due to the accumulation of electron microscopic load.

Figure 2d, e, refers to the sample P2. In this image, taken at a magnification of 10,000 times, the fine and coarse particles of platinum, all of which are spherical, are well visible. The sedimentation voltage of this pulsed sample is lower and the platinum layer does not cover the full FTO surface. In Figure 2, the part marked in the previous figure is displayed at a magnification of 50,000 times. Extremely fine particles of platinum and two relatively large particles, all of which are spherical, are visible. Particles have different sizes and apparently at the growth stage. The surface of this sample was excellent, but unclear and dark. You can see the dimensions of these particles in this shape. In this image, platinum particles are visible from 56 to 344 nm. With greater magnification, the surface of the particles of platinum is visible. The surface of each particle consists of infinitely many fine particles of platinum, each of which is single. According to these images, it is clear that in samples P, the coating contains platinum nanoparticles. However, the goal of this project is to apply coating on graphite, and success at this stage is not enough.

For GP1, the first image, Figure 3a, is magnified by 1000 times. In the image of the graphite surface, where particles of platinum are not recognizable on its surface, some areas are unevenly visible. Expecting to see nanometric particles in this magnification is futile. However, due to the unspecified, a white streak is seen in the middle of the image.

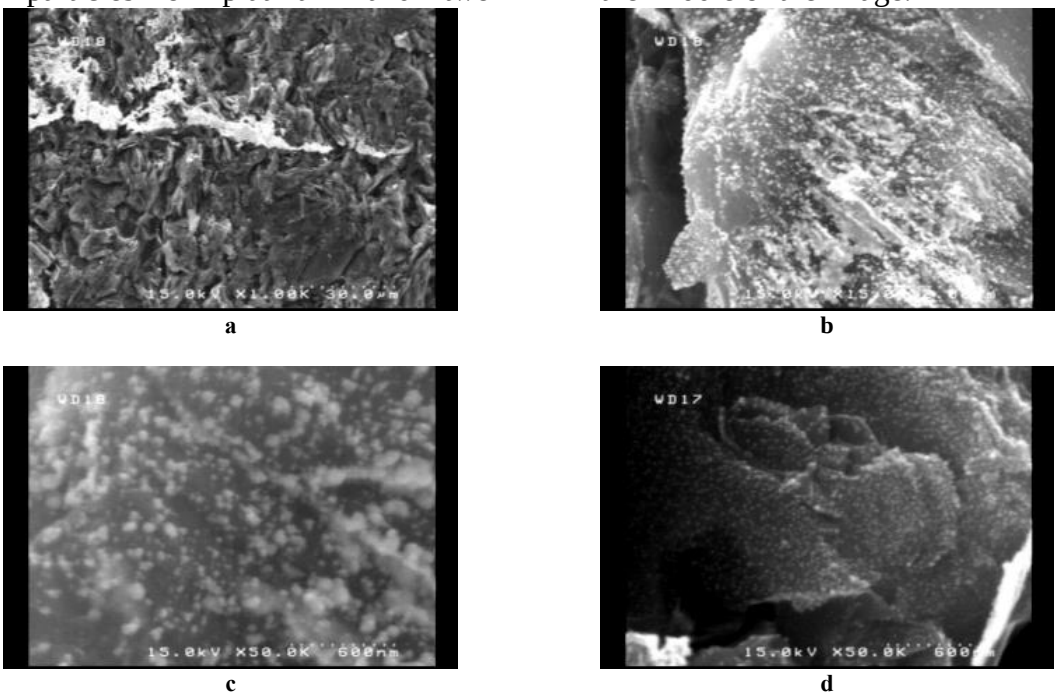

Fig. 3. Figure of the field emission scanning electron microscope (FESEM) from the GP1 specimen. Zoom 1000 x (A), 15000 x (B), 50,000x(C) of GP2 sample. Magnification is 50,000 x (d).

In Figure 3b, which is shown with a magnification of 15,000 times, the surface of graphite deposited on the platinum particles is well known, although the more interlayer surfaces are graphite without deposition, single platinum particles are definitely on its surface. In the middle areas of the image (where it is marked with red circles), fine particles are mixed together and coarse particles are created. Agglomeration is also observed in areas. At a magnification of 50,000 times the image of 3C, platinum particles are still tiny. Despite the conductivity of graphite, the accumulation of load in this sample was very severe and allowed to go to higher magnifications hardly. That's why the image is blurry. In Fig. 3C, too many platinum particles are cut. Particle sizes in this sample are estimated at a maximum of 30 nm. Also, Figure 3d shows the image of the field emission scanning electron microscope (FESEM) from the GP2 specimen. The magnitude of the 50,000-fold increase shows the island's growth of platinum particles (in the range of several nanometers in the range of 10 to 20 nanometers) in this image, although the lower density of these particles indicates a limited sedimentation rate for these particles. The result with the platinum level calculations, cyclic curves can also be verified.

The FTO sample of the atomic microscope was also used to confirm the SEM data. AFM images were obtained from the samples, which was not possible due to the porous graphite structure. This was done for the P2 sample. Two images were prepared for the P2 sample, one in the size of 4 μ m × 4 μ m and another 2 μ m × 2 μ m. Using AFM, in addition to topography, fuzzy properties can also be determined, because the different genus of the atom under the probe causes the input signal to vary. Platinum The bulges seen in the brighter topographic image correspond to the prominences in the fuzzy image, which represent particles of platinum. Given that the platinum cover is pure, and according to SEM images, expect this behavior to be logical. Meanwhile, these areas have a circular cross section. At the bottom of the image, the particles of platinum are clearly visible alongside. Now, these regions with circle cross-section (spheres) have different fuzzy contrast, that is, they have different sexes. These are the same particles of platinum.

In Figure 4 a and b, the topographic and fuzzy signals are compared. The bulges seen in the brighter topographic image correspond to the prominences in the fuzzy image, which represent particles of platinum. Given that the platinum cover is pure, and according to SEM images, expect this behavior to be logical. Meanwhile, these areas have a circular cross section. At the bottom of the image, the particles of platinum are clearly visible alongside. Now, these regions with circle cross-section (spheres) have different fuzzy contrast, that is, they have different sexes. These are the same particles of platinum. In the fuzzy image due to the fuzzy contrast, small particles of platinum also appear in the topographic image of the valleys.

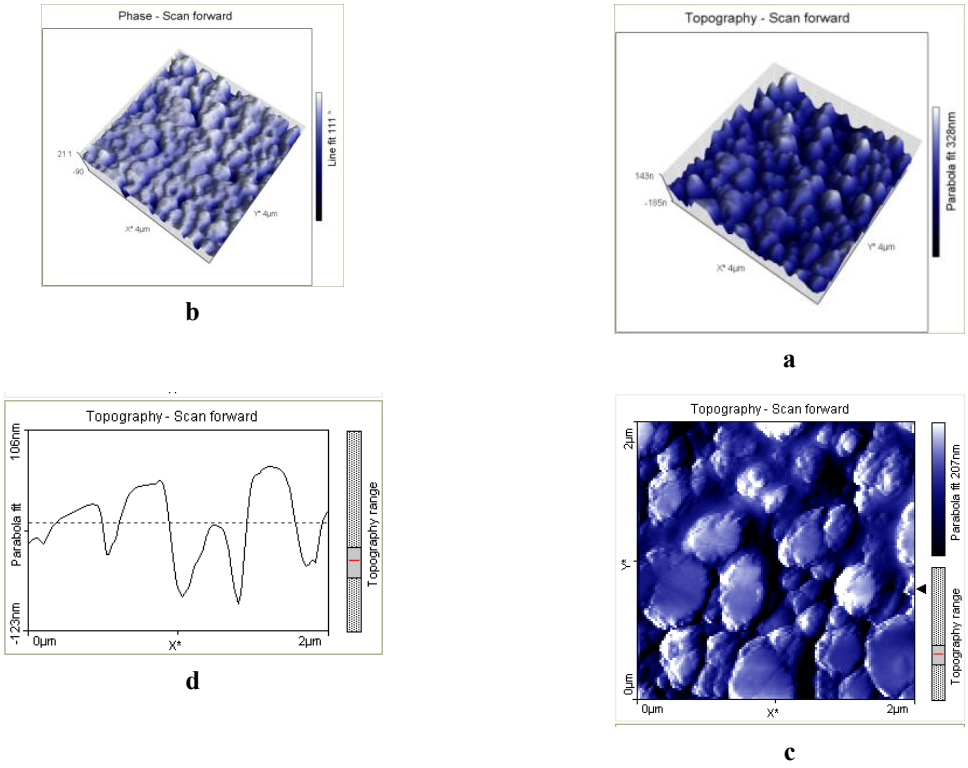

Figure 4. The atomic force microscope image (AFM) of sample P2. The dimensions of the image are 4 μ m × 4 μ m, the height dimension is also displayed in this 3D image; here the fuzzy image (A) and the topographic image (B) of the image are 2 μ m × 2 μ m, in the topography (C), the height profile of the drawing (D)

The image of 4C is four times larger than the previous one and is also here adapted. Given this shape, it cannot be said that the particles are definitely spherical. They may be disc shaped. The height profiles in Fig. 4d shows, according to the profile, the particle height changes gradually and slightly on each single particle. According to this picture, the probability of spherical particles is greater than their disks. In this image, the size of a large particle is 303 nm. This result is consistent with the SEM images for the P2 sample.

The distribution of platinum in various coating surfaces using isotherms and the absorption heat associated with the presence of platinum in the coating is summarized in Table 2. [The results show that the GP1 specimen has a higher heat and coating surface that can be compared and verified according to the results of cyclic voltammetry and electron microscopic images.

Table 2. Type of coatings and Pt Concentration, %coverage and H_2adsorption energy

Sample name	% coverage	Heat od adsorption (Kj/mol)
P2	16.6	**92**
GP2	9.8	**86**
P1	12.1	**89**
GP1	26.9	**93**

Conclusions

According to the results, it can be concluded that optimal cyclic platinum conditions were found on FTO and graphite glass. The results of microscopy and voltammetric data and isotherms show the stability of absorption and the amount of platinum in the synthesized samples in accordance with the working conditions. Graphitic specimen GP1 provides the highest sediment rate and the highest level of platinum, which is very suitable for the use of fuel cell electrode. Also, the platinum sediment morphology was spherical in all cases. In cases where the growth rate was high, growth was rapidly converted to three-dimensional growth, and eventually caused the platinum layer to separate from the substrate. This was associated with platinum agglomeration. The platinum sediment on the FTO does not have much stability and is easily detached. In the case of pulsed samples on graphite, the surface layer stability was higher.

References

[1] Srinivasan. S, Mosdale. R, Stevens. P and Yang. C, Annual Review of Energy Environment, 1999, 20.

[2] Mateo. J. J, Tryk. D. A, Cabrera. C. R and Ishikawa. Y, Molecular Simulation, 2008, 34, 1065,10-15.

[3] EG&G Technical Services Inc., in Fuel Cell Handbook, U.S. Department of Energy Office of Fossil Energy National Energy Technology Laboratory, 2005, 15-45.

[4] Larminie. J and Dicks. A, in Fuel Cell Systems Explaind, 2nd ed., Chichester, John Wiley, 2003, 67-119.

[5] Hoogers. G, in Fuel Cell Technology Handbook, CRC, 2003, 137-160.

[6] Hideya Okamoto, President & CEO , Tanaka Holdings Co.,Ltd, 2010.

[7] Baumgarner. M. E and Raub. C. J, Platinum metal Review, 1988, 32. 4, 188.

[8] Zelenovic-Ribic. L, Tripkovic. A and Rafailovic. L, Acta Agriculturae Serbia,2005, 19. 33.

[9] Xiao. H, Blanar. T and Manoharan. R, Rosemount Analytical Inc. Orrville, Ohio, 2010, 44667.

[10] Saltykova. N. A, Journal of Minerals and Metals, 2003 , 201, 39. 1-2.

[11] Dryfe. R. A. W, Walter. E. C and Penner. R. M, European Journal of Chemical Physics and Physical Chemistry (ChemPhysChem), 2004, 5,1879.

[12] Hong. Y. H and Tsai. Y. C, Journal of Nanomaterials, online edition, 2009, 1.

[13] Zubeimendi. J. L, Vazquez. L, Ocon. P, Vara. J. M, Triaca. W. E, Salvarezza. R. C and Arvia. A. J, Journal of Physical Chemistry, 1993, 97, 5095.

[14] Anpo. M, Kamat. P, Uner. D, Book Chapter of environmentally design catalysts, Springer, Germany, 2009.

[15] Flores Araujo. S. C, Electrochemical Study of Under-Potential Deposition Processes On Transition Metal Surfaces, Austin: University of Texas, 2006.

[16] Mateo. J. J, Tryk. D. A, Cabrera. C. R and Ishikawa. Y, Molecular Simulation, 2008 , 1065, 34. 10-15.

[17] Stevanović. S, Tripković. D, Kowal. A, Minić. D, Jovanović. V. M,

Tripković. A, J. Serb. Chem. Soc. 2008 73, 845,8–9.

[18] Tripkovic. A. V, Gojkovic. S. Popovic. L. K. D and Lovic. J. D, Journal of Serbian Chemical Society, 2006, 71. 12,1333.

[19] Lee. I. S, Chan. K. Y and Philips. D. L, Japanes Journal of Applies Physics, 2004, 43, 767.

[20] Hill. A C, Patterson. R, Sefton. J. P and Columbia. M. R, " Langmuir, 1999, 15, 11, 4005.

Communications In Catalysis
Vol. 1, No. 2, 2024, pp.15-22
DOI: 10.22049/CIC.2018.26245.1020

Azarbaijan Shahid Madani University

Molecular iodine-catalyzed combinatorial library synthesis of 2-amino-3-cyano-4*H*-pyran derivatives at ambient temperature

Adeleh Moshtaghi Zonouz*, Davoud Moghani

Department of Chemistry, Faculty of Science, Azarbaijan Shahid Madani University, Tabriz, Iran.

*Corresponding author. Fax: +984134327541

E-mail address: adelehmz@yahoo.com

Received: 2024-08-12, Revised: 2024-09-06, Accepted: 2024-09-22

Abstract

An efficient and simple synthesis of some 2-amino-3-cyano-4*H*-pyran derivatives was developed via the one-pot and three-component reaction of aldehydes, ethyl acetoacetate, and malononitrile in the presence of ammonium acetate at room temperature using catalytic amount of iodine. The key advantages of this method are the easy access to various substituted 2-amino-3-cyano-4*H*-pyran derivatives, short reaction times and high yields.

Keywords: 2-amino-3-cyano-4*H*-pyrans, one-pot reaction, multi-component reaction, molecular iodine

Introduction

2-Amino-4*H*-pyran derivatives represent an important class of compounds. They are often used in cosmetics and pigments, and utilized as potentially biodegradable agrochemicals [1-3]. Polyfunctionalized 4*H*-pyrans also constitute a structural unit of many natural products [4, 5] and biologically interesting compounds which possess various pharmacological activities, such as antiallergic [6], antitumor [7], and antibacterial [8-12]. 4*H*-Pyran derivatives are also potential calcium channel antagonists [13] which are structurally similar to biologically active 1,4-dihydropyridines (1,4-DHPs).

Generally, 2-amino-4-aryl-3-cyano-4*H*-pyrans are synthesized by the cyclization of arylidenemalononitriles and active methylene compounds in the presence of organic bases such as piperidine [14], pyridine [15], triethylamine [16, 17]. Most of these methods involve the use of volatile solvents and require longer reaction time (~ 2 h) and present with the difficulty in recovering the catalyst. Recently, one-pot synthesis of these compounds has been reported using Mg/La mixed oxide [18] and MgO [19, 20] as the basic catalyst. Also, SiO_2 NP-catalyzed (silica nanoparticles, SiO_2 NPs) one-pot synthesis of 4*H*-pyran derivatives has been reported [21]. More recently, we reported the multicomponent synthesis of 2-amino-4*H*-pyran derivatives in aqueous medium [22-24].

Thus, in view of the importance of this class of compounds, the development of a simple, efficient and versatile method for the preparation of 2-amino substituted 4*H*-pyrans is an active area of research and there is a scope for further improvement towards milder reaction conditions and higher product yields.

In recent years, the use of molecular iodine as an inexpensive, non-toxic, and readily available catalyst for various organic transformations to afford the corresponding products in excellent yields has received considerable attention. The mild Lewis acidity associated with iodine has enhanced its usage in organic synthesis to realize several organic transformations using stoichiometric levels to catalytic amounts. Owing to numerous advantages associated with this eco-friendly element, iodine has been explored as a powerful catalyst for various organic transformations [25-28].

All these facts prompted us to use catalytic amount of molecular iodine in the multi-component reaction for a combinatorial synthesis of ethyl 2-amino-4-aryl-3-cyano-6-methyl-4*H*-pyran-3-carboxylates **2a-l** under ambient conditions.

Experimental

Typical procedure: Preparation of ethyl 2-amino-3-cyano-6-methyl-4-(2-methylphenyl)-4*H*-pyran-5-carboxylate *2j*

A 10 mL round-bottomed flask was charged with 2-methylbenzaldehyde **1j** (0.12 mL, 1 mmol), malononitrile (0.066 g, 1 mmol), ethyl acetoacetate (0.136 mL, 1 mmol), ammonium acetate (0.115 g, 1.5 mmol), iodine (0.038 g, 0.15 mmol) and a few drops of ethanol (5-6 drops). The mixture was then stirred at room temperature under an open atmosphere till the completion of reaction as indicated by TLC (Thin Layer Chromatography) (55 min). The precipitated solid was filtered, and washed with water. The crude product was recrystallized from ethanol to

give **2j** as white crystals (0.229 g, 77 % yield). mp 140-141 °C; IR (KBr) $\overline{\nu}$ = 3426 (s), 3332 (s), 3202 (m), 2194 (s), 1690 (s), 1647 (m), 1608 (m), 1370 (m), 1259 (s), 1061 (s), 742 (s) cm^{-1}; ^1H NMR (300 MHz, $CDCl_3$): δ = 1.03 (t, *J* = 7.20 Hz, 3H, CH_3 ester), 2.38 (s, 3H, CH_3-6), 2.49 (s, 3H, CH_3), 3.98 (m, 2H, CH_2 ester), 4.51 (br, s, NH_2), 4.77 (s, 1H, C(4)-H), 7.10 (m, 4H, Ar-H) ppm; ^{13}C NMR (75 MHz, $CDCl_3$): δ = 13.91 (CH_3 ester), 18.34 (CH_3-6), 19.27 (CH_3), 34.15 (C-4), 60.60 (CH_2 ester), 61.71 (C-3), 108.04 (C-5), 119.12 (CN), 126.59, 126.85 (C-4´, 5´), 127.87, 130.37 (C-3´, 6´), 135.21 (C-1´), 142.47 (C-2´), 157.02, 157.42 (C-2, 6), 165.91 (CO) ppm; MS (70 eV): m/z (%) = 298 (18.40) [M^+], 269 (13.89), 253 (6,69), 225 (8.35), 207 (100), 179 (28.92), 161 (15.53); ($C_{17}H_{18}N_2O_3$) Calcd.: C 68.44, H 6.08, N 9.39; found: C 68.65, H 5.98, N 9.20. X-ray data: CCDC 798881; $C_{17}H_{18}N_2O_3$, Mw = 298.33 g/mol, Triclini**c** P-1 (No. 2)**,** a = 8.563(2), b = 9.385(3), c = 10.605(3) Å, α= 106.41(3)˚, β = 101.11(4) ˚, γ = 102.90(3)˚, V = 766.4(4) $Å^3$, Z = 2, ρcalcd = 1.293 g/cm^3, μ(MoK_α) = 0.71069 Å), colorless, transparent, crystal dimensions = 0.40 × 0.48 × 0.72 mm, 3401 independent reflections.

Results and Discussion

In the efforts to develop an efficient and environmentally benign methodology for the synthesis of 2-amino substituted 4*H*-pyrans (**2**), we initiated our studies through a three-component reaction between benzaldehyde **1a** (1 mmol), ethyl acetoacetate (1 mmol), and malononitrile (1 mmol) in a few drops of ethanol at room temperature. No reaction was observed. Then ammonium acetate (1.5 mmol), as a basic catalyst, was added to the reaction mixture. After 2 hours, only 24% of product **2a** was obtained after recrystallization of the crude product from ethanol. Despite using a high quantity of ammonium acetate, 1,4-dihydropyridine was not detected as the product. We also carried out the reaction at refluxing temperature in ethanol for thermal decomposition of ammonium acetate to ammonia which can enhance the formation of pyridine rather than the pyran; again, in this case the pyran derivative was formed rather than the pyridine derivative. To improve the product yield, based on the literature survey [27], iodine was used in catalytic amount (15 mol%) and the reaction was carried out under similar conditions. To our surprise, a significant improvement in the yield of product **2a** (91%) was observed. The reaction was also carried out under similar conditions in the presence of catalytic amount of iodine without using ammonium acetate, but no reaction was observed. Using ammonium acetate and iodine are complementary to each other, because when ammonium acetate was used as a basic catalyst, low yield of pyran products was obtained (<25%), and when the reaction was carried out under similar conditions in the presence of catalytic amount of iodine without using ammonium acetate, no reaction was observed. Hence, the presence of one chemical enhances the effects of the second, and therefore, ammonium acetate and iodine have a synergistic effect in this methodology. In this case ammonium acetate acts as a basic catalyst, and the acidity of iodine

makes it capable of binding with the aldehyde carbonyl oxygen, thereby increasing the reactivity of the parent carbonyl compounds.

Thus halogen-bond activation mode [29, 30] is proposed for this iodine-catalyzed reaction. This mode of activation can catalyze both Knovenagel condensation and Michael addition reactions (Scheme 1).

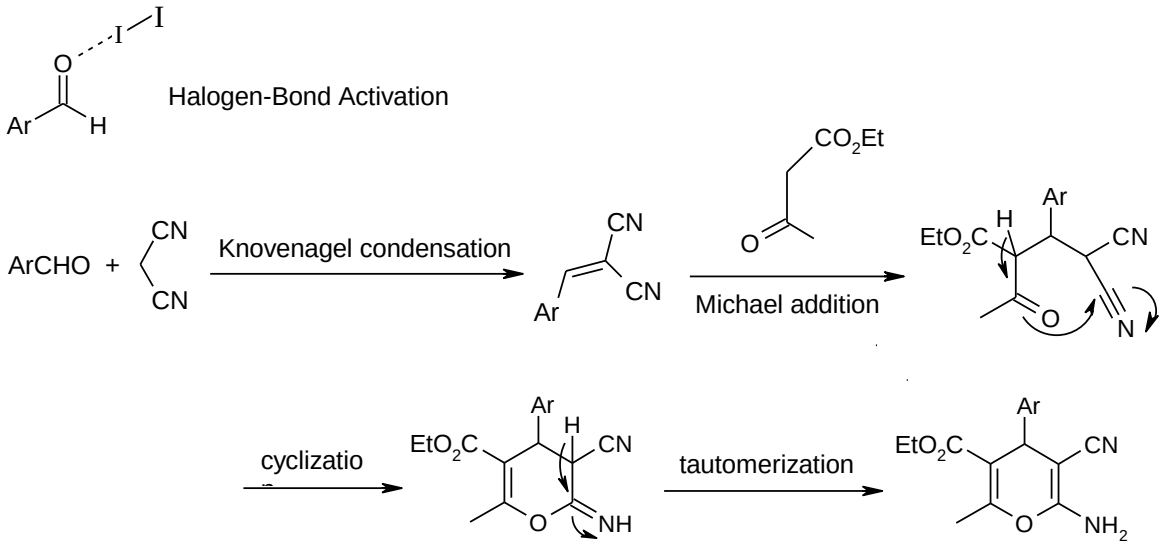

Scheme 1. Proposed mechanism for the formation of products **2**

The improved conditions were then applied to a range of aldehyde substrates. Both electron-poor and electron-rich aldehydes were well tolerated. The results with different aldehydes are depicted in table 1. It was evident that different aromatic aldehydes with ethyl acetoacetate and malononitrile could be converted to the corresponding products in good to excellent yields in the presence of ammonium acetate and catalytic amount of iodine (15 mol%) at room temperature. The structure of **2j** was determined by X-ray crystallographic study [31]. Figure 1 shows the structure and the atomic numbering scheme used for the compound **2j**.

Selected bond distances and angles for compound **2j** are listed in tables 2 and 3 respectively.

The X-ray structural analysis of **2j** (Figure 1) shows that the 4*H*-pyran ring is in a flattened boat conformation, with the 4-aryl substituent in the pseudo axial position and orthogonal to the plane of the 4*H*-pyran ring. Moreover the methyl substituent in the phenyl ring lies on the same side as the C4-hydrogen on the 4*H*-pyran ring (synperiplanar, *sp*); thus crystal structure of compound **2j** shows the *sp* conformer. Also the carbonyl group ester is *trans* to the double bond of the 4*H*-pyran.

Table 1. Iodine-catalyzed three-component synthesis of 2-amino-4-aryl-3-cyano-4*H*-pyran derivatives[a].

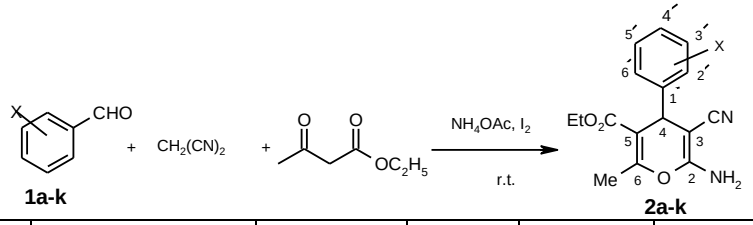

Entry	Aldehyde	Time (min)	Product	Yield (%)	Mp (˚C)
1	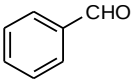	110	**2a**	91[b]	190-192
2	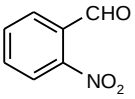	45	**2b**	97[b]	177.5-178.5
3	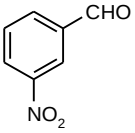	55	**2c**	99[b]	187-188
4	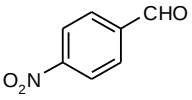	75	**2d**	80[c]	175-176
5	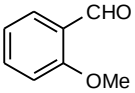	90	**2e**	72[c]	196-197
6	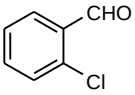	25	**2f**	99[b]	191-192
7	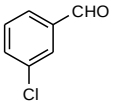	70	**2g**	82[c]	180-180.5
8	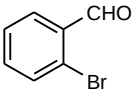	35	**2h**	99[b]	183-184
9	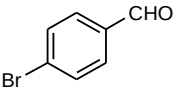	100	**2i**	80[c]	180-181
10	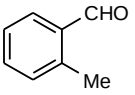	55	**2j**	77[c]	140-141
11	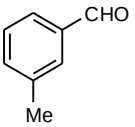	65	**2k**	79[c]	176-177
12	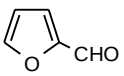	45	**2l**	85[c]	203-204

[a]All reactions were conducted using aldehyde (1 mmol), ethyl acetoacetate (1 mmol), malononitrile (1 mmol), ammonium acetate (0.15 mmol), and molecular iodine (15 mol %) in a few drops of ethanol at room temperature. The structures of compounds **2a-l** were confirmed by the comparison of melting points and spectral data obtained in this study with those reported in the literature [22]. [b] Crude isolated yields. [c] After recrystallization.

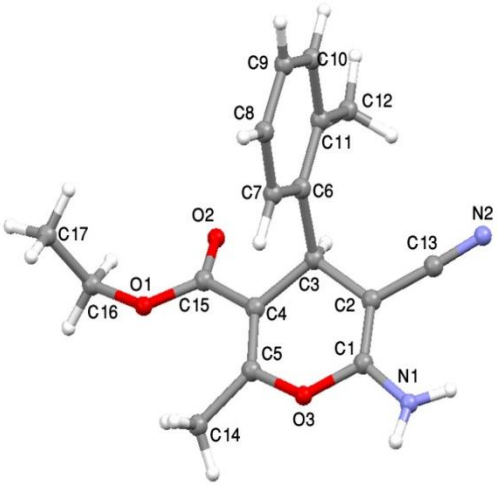

Figure 1. Crystal structure of ethyl 2-amino-3-cyano-6-methyl-4-(2-methylphenyl)-4*H*-pyran-5-carboxylate **2j**.

Table 2. Bond lengths (Å) of the compound $C_{17}H_{18}N_2O_3$.

N1-C1	1.3425 (19)	C3-C6	1.534 (2)
N2-C13	1.149 (2)	C4-C5	1.332 (2)
O1-C15	1.334 (2)	C4-C15	1.488 (2)
O1-C16	1.459 (2)	C5-C14	1.479 (3)
O2-C15	1.193 (2)	C6-C7	1.388 (2)
O3-C1	1.3624 (19)	C6-C11	1.390 (2)
O3-C5	1.3945 (17)	C7-C8	1.395 (2)
C1-C2	1.344 (2)	C8-C9	1.366 (3)
C2-C13	1.412 (2)	C9-C10	1.375 (3)
O1-C16	1.459 (2)	C10-C11	1.398 (2)
C2-C3	1.5181 (19)	C11-C12	1.497 (3)
C3-C4	1.504 (2)	C16-C17	1.430 (3)

Table 3. Bond angles (deg) of the compound $C_{17}H_{18}N_2O_3$.

C1-O3-C5	119.89 (12)	C7-C6-C11	119.40 (15)
N1-C1-C2	128.14 (15)	C7-C6-C3	118.67 (16)
N1-C1-O3	110.41 (14)	C11-C6-C3	121.82 (14)
C2-C1-O3	121.44 (12)	C6-C7-C8	120.58 (19)
C1-C2-C13	119.65 (13)	C9-C8-C7	120.04 (19)
C1-C2-C3	122.09 (13)	C8-C9-C10	119.78 (17)
C13-C2-C3	117.81 (14)	C9-C10-C11	121.3 (2)
C4-C3-C2	109.77 (13)	C6-C11-C10	118.92 (17)
C4-C3-C6	112.59 (12)	C6-C11-C12	121.87 (15)
C2-C3-C6	110.14 (12)	C10-C11-C12	119.20 (18)
C5-C4-C15	124.74 (15)	N2-C13-C2	177.34 (17)
C5-C4-C3	122.42 (13)	O2-C15-O1	122.96 (14)
C15-C4-C3	112.81 (14)	O2-C15-C4	121.94 (16)
C4-C5-O3	121.33 (14)	O1-C15-C4	115.10 (15)
C4-C5-C14	130.93 (14)	C17-C16-O1	110.85 (19)
O3-C5-C14	107.74 (14)		

Conclusion

In summary, the one-pot three-component reaction protocol developed in the present study offers a fast and an efficient method for the synthesis of 2-amino substituted 4*H*-pyrans at room temperature. The experimental procedure is simple and represents an attractive alternative to existing methods. This reaction protocol conforms to several green chemistry principles coupled with the potential for developing combinatorial libraries.

Supplementary material

Crystallographic data for the structural analysis has been deposited with the Cambridge Crystallographic Data Center (CCDC, No. 798881 for compound **2j**). The above-mentioned data may be obtained free of charge from the Director, CCDC, 12, Union Road, Cambridge CB2 1EZ [FAX +44 (1223) 336-033] or E - mail: deposit@ccdc.cam.ac.uk or http://www.ccdc.cam.ac.uk.

Acknowledgements

The authors acknowledge the research office of Azarbaijan Shahid Madani University for financial support. We are also grateful to Dr. Michael Serafin from the institute of inorganic chemistry of the Giessen University for X-ray analysis.

References

[1] Ellis. G. P, Weissberger. A, Taylor. E.C, The chemistry of heterocyclic compounds. In Chromenes, Chromanes and Chromeones. Wiley: New York. 1977, P.13.

[2] Abdel Galil. F. M, Riad. B.Y, Sherif. S.M, Elnagdi. M. H, Chem. Lett. **1982,** 11, 1123.

[3] Hafez. E. A, Elnagdi. M.H, Elagamey. A. A, El-Taweel. F. A, Heterocycles, 1987,26, 903.

[4] Kuthan. J, Adv. Heterocycl. Chem, 1983, vol. 34, 145.

[5] Hatakeyama. S, Ochi. N, Numata. H, Takano. S. J, Chem. Soc. Chem. Commun, 1988,17, 1202.

[6] Witte. E. C, Neubert. P, Roesoh. A, Ger Offen. DE, 1986, 3427985.

[7] Wang. J , Liu. D, Zhang. Z. J, Shan. S, Han. X, Srinivasula. S.M, Croce. C. M, Alnemri. E.S, Huang. Z, Proc. Natl. Acad. Sci. U.S.A, 2000, 97, 7124.

[8] El-Saghier. A. M. M, Naili. M. B, Rammash. B. Kh, Saleh. N. A, Kreddan. K. M, Arkivoc xvi, 2007,83.

[9] Kumar. R. R, Perumal. S, Senthilkumar. P, Yogeeswari. P, Sriram. D, Bioorg. Med. Chem. Lett, 2007,17, 6459.

[10] Fairlamb. I. J. S, Marrison. L. R, Dickinson. J. M, Lu. F.J, Schmidt. J. P, Bioorg. Med. Chem.2004,12, 4285.

[11] Aytemir. M. D, Erol, D. D, Hider. R. C, Özalp. M, Turk, J. Chem, 2003, 27, 757.

[12] Kidwai. M, Saxena. S, Khan. M. K. R, Thukral. S. S, Bioorg. Med. Chem. Lett, 2005,15, 4295.

[13] Suarez. M, Salfran. E, Verdecia. Y, Ochoa. E, Alba. L, Martin. N, Martinez. R, Quinteiro. M, Seoane. C, Novoa. H, Blaton. N, Peeters. O. M, De Ranter. C, Tetrahedron, 2002, 58, 953.

[14] Martin. N, Pascual. C, Seoane. C, Soto. J, L.Heterocycles.1987,26, 2811.

[15] Harb. A. F, Hesien. A. M, Metwally. S. A, Elnagdi. M. H, Liebigs Ann. Chem,1989, 585.

[16] Zayed. S. E, Abou Elmaged. E. I, Metwally. S. A, Elnagdi, M. H, Collect. Czech. Chem. Commun.1991, 56, 2175.

[17] Elnagdi. M. H, Adbel-Motaleb. R. M, Mustafa. M. J, Heterocycl. Chem, 1987,24, 1677.

[18] Seshu Babu. N, Pasha. N, Venkateswara Roa. K. T, Sai Prasad.

P. S, Lingaiah. N, Tetrahedron Lett,2008,49, 2730.
[19] Kumar. D, Reddy. V. B, Mishra. B. G, Rana. R. K, Nadagouda. M. N, Varma. R. S, Tetrahedron, 2007, 63, 3093.
[20] Kumar. D, Reddy, V. B, Sharad. Sh, Dube. U, Kapur. S, Eur. J. Med. Chem, 2009,44, 3805.
[21] Banerjee. S, Horn. A, Khatri. H, Sereda, G, Tetrahedron Lett, 2011,52, 1878.
[22] Moshtaghi. Z. A, Eskandari. I, Moghani. D, Chem. Sci. Trans, 2012, 1, 91.
[23] Moshtaghi. Z. A, Eskandari. I, Khavasi. H. R, Tetrahedron Lett, 2012, 53, 5519.
[24] Moshtaghi. Z. A, Moghani. D, Okhravi. S, Current Chem. Lett, 2014, 3, 71.
[25] Zolfigol. M. A, Salehi. P, Khorramabadi-zad. A, Shayegh. M, J. Mol. Catal. A, 2007, 261, 88.
[26] Yadav. J. S, Reddy. B. V. S, Rao. C, Reddy. V. M, J. Synthesis, 2003,247.
[27] Bhosale. R. S, Magar. Ch. V, Solanke. K. S, Mane. S. B, Choudhary. S. S, Pawar. R. P, Synth. Commun, 2007,37, 4353.
[28] Ko. S, Sastry. M. N. V, Lin. C, Yao. C. F, Tetrahedron Lett, 2005,46, 5771.
[29] Von der Heiden. D, Bozkus. S, Klussmann. M, Breugst. MJ, Org. Chem, 2017, 82 (8), 4037.
[30] Breugst. M, Von der Heiden. D, Chem. Eur. J, 2018, 24, 9187.
[31] (a) Sheldrick. G.M, SHELXS-86, Program for the Solution of Crystal Structures, Universität Göttingen, (b) Sheldrick. G.M, SHELXL-1986,93, Program for Crystal Structure Refinement, Universität Göttingen, 1993.

Communications In Catalysis
Vol. 1, No. 2, 2024, pp.23-33
DOI: 10.22049/CIC.2018.26259.1021

Azarbaijan Shahid Madani University

Studying the role of sodium hydrogen sulfate stabilized on nanosilica for preparing some coumarin derivatives in the solution and under solvent-free conditions

Abdolreza Abri[a,]*, Mostafa Ebrahilou[b]

[a,b]Chemistry Department, Faculty of Science, Azarbaijan Shahid Madani University, Tabriz, Iran

*Corresponding author. Tel.: +98 (41) 31452187; Fax number: +98 (41) 34327541

E-mail: ar.abri@azaruniv.edu

Received: 2024-09-10, Revised: 2024-10-18, Accepted: 2024-11-20

Abstract

Coumarin and its derivatives are the most important components of several bioactive compounds such as anticoagulants, anti-HIVs, anti-tumors, anti-oxidants, anti-anxieties, anti-inflammatories, hypnotics, helminthicides, and insecticides. Derivatives of 2H-Chromen-2-one, or coumarins, are synthesized mainly through pechmann condensation reactions. This condensation involves phenol derivatives and β -ketoesters that occur in the presence of an acidic catalyst under reflux, but the yield of coumarin derivatives obtained in this method is very low and the reaction time is long. Although a lot of modified methods have been proposed, each one of them has some disadvantages, such as hard conditions, low efficiency, long time, expensive reagents, formation of byproducts, and difficulty of recycling and reusing the catalyst. In this research, an efficient method is offered for synthesis of some coumarin derivatives using pechmann condensation reactions in the presence of phenol and ethyl acetoacetate with sodium hydrogen sulfate stabilized on nanosilica as the catalyst. This method has advantages, such as high yields, short reaction time, simple purification.

Keywords: Pechmann condensation, sodium hydrogen sulfate, nano silica, coumarins, sol-gel

Introduction

Coumarin or 2H-chromen-2-one is a colorless and crystalline substance belonging to the benzo-pyrene family and mostly is found as phenol in several herbs, especially with high concentrations in tonka beans and vanilla. This compound is used as a freshener in perfumery and also as an additive in food but it is banned due to liver toxicity. Coumarin was also used as an anticoagulant like dihydrochloride after laboratory synthesis in 1868. Warfarin is a trademark of this drug (containing coumarin), which is used as an anticoagulant [1,2]. Among the pharmaceutical activities of coumarin and its derivatives, hypnotic activity, helminthicide, insecticide and anticoagulant, anti-inflammatory, anti-tumor, and antibacterial can be mentioned [3-6].

Due to the importance of coumarin and its derivatives, different methods have been proposed for the synthesis of these compounds; among these methods, the condensation reactions of pechmann, perkin, reformatsky, witting, claisen, and others can be mentioned. Pechmann condensation reaction has been interesting due to its convenient synthesis. These reactions are carried out with phenolic derivatives and β- ketoesters in the presence of acidic reagents such as chloric acid, sulfuric acid, acetic acid, etc. These reactions are not considered extensively due to the long reaction time, high temperature, and contamination caused by the excessive acid in the environment.

During recent years, Lewis acids such as $AlCl_3$, Yb $(OTf)_3$, $ZrCl_4$, etc. have been utilized, some of which are sensitive to moisture and require specific conditions for reaction. Moreover, their reaction needs high temperature and long time to be carried out. Researchers have recently used catalysts containing metallic hydrogen sulfate as a source of protonated acids and lewis acids, which are inexpensive and stable, and their reactions are carried out in heterogeneous environments [7-9].

Importance of green chemistry has led to creation of environmentally friendly methods for synthesis of chemical compounds. In this regard, the use of solid acids as heterogeneous catalysts has expanded due to their easy application, convenient separation, reusability, and prevention of chemical waste production [10-13]. Among these, bronsted acidic nanocatalysts functionalized with sulfonic acid (SO_3H) have shown high activity in organic reactions and are a good alternative for mineral liquid acids [14-20]. Unlike homogeneous catalysts, heterogeneous catalysts are easily separated from the reaction mixture and do not cause impurities. In order to compensate lack of active surface in these compounds, using a substrate as a support is essential for catalysts.

Although the active surface of nanocatalysts is much higher than conventional catalysts, the active surface of a nanocatalyst is always lower than a homogeneous catalyst (a homogeneous catalyst with its dissolution is in full contact with the reaction content). In contrast, catalytic nanoparticles are not solvated in the solution due to their larger dimensions than those of homogeneous catalyst particles, and can be easily separated. High active surface along with the ability to separate the catalyst at the

end of the reaction causes formation of a bridge between homogenous and heterogeneous catalysts. The complex manufacturing process of some nanocatalysts may be considered costly, but this can be neglected as the amount of catalyst and the energy and time needed to react decrease in the nanotechnology.

Experimental

Chemicals and instruments

All chemicals and solvents used in this study are purchased from Merck and Aldrich Companies and have been used without further purification. In order to investigate the reaction progress, a thin film of chromatography (TLC) with an aluminum plate and silica gel F254 60 and ultraviolet light have been used. The melting temperature of the synthesized products was measured with the thermoscientefic melting point of 9100. The IR spectrum has been reported by the bruker infrared spectrometer model PS15 and using a potassium bromide pallet. Also, ^{1}H NMR spectra were obtained by the broker spectrospin with the power of 400 MHz and ^{13}C NMR spectra were recorded with a 75 MHz bruker spectrospinn device.

In this research, all reactions (both with solvent and without solvent) were carried out at room temperature under mild conditions, and all solvents used were carefully dried using standard methods.

Nano Silica Preparation Method

100 ml of methanol and 750 ml of 25% ammonia are poured in a 250 ml balloon. Then, 1.92 g of distilled water is added to the mixture. After 15 minutes of stirring in the magnetic stirrer, 10.41 g of the tetraethoxysilane compound is added dropwise. After 3 days, the resulting unclear mixture is extracted using petroleum ether. Then, using a centrifuge, a gelatinous compound is formed, which is obtained in the form of a white powder by drying at 60-70 ° C nanosilica.

preparation of $NaHSO_4$ .SiO_2 (nano)

0.1 g of nanosilica is mixed with 0.2 g of the $NaHSO_4.H_2O$ solution and 1 ml of distilled water was added to it and thein it was stirred for 2-3 hours. The mixture is then dried at 120 ℃ for 2-3 hours and the catalyst is obtained.

General Method for the Synthesis of Coumarin Derivatives

In a 10 ml balloon, 1 ml of phenol derivative, 1 ml of ethyl acetoacetate, and 0.05 gr of sodium hydrogen sulphate stabilized on the nanosilica were mixed and about 3 ml of acetonitrile was added to it. The reaction mixture was stirred at room temperature and the reaction progress was controlled by a thin layer of chromatography in an n-hexane and ethyl acetate solvent. After completion of the initial phenol combination and separating the catalyst, some ice was crushed and the reaction mixture was poured onto it, and then it was stirred and filtered. After evaporation of the solvent under the filter, the obtained solid is recrystallized using hot ethanol. The remaining solids on a filter are dried and rinsed with a completely cold ethanol and then, they are filtered.

Spectral data of some resulted products

Table 4, row 11

4,5,6,7-Tetramethyl-2H-chromen-2-one (11): Yellow solid; m.p.: 164–165 °C; IR (KBr) ν_{max} (cm^{-1}): 1673 (ester C=O stretch), 1604 (C−C=C stretch); ^{1}H-NMR (DMSO-d6) δ: 2.14 (s, 3H, CH_3), 2.22 (s, 3H, CH_3), 2.32 (s, 3H, CH_3), 2.40 (s, 3H, CH_3), 6.24 (m, 1H), 7.23 (s, 1H); ^{13}C-NMR (DMSO-d6) δ: 14.3, 17.5, 21.6, 23.5, 114.3, 117.2, 121.6, 125.5, 131.5, 133.8, 152.2, 158.5. MS (m/z): 202 (M+); Anal. Calcd for $C_{13}H_{14}O_2$: C, 77.30; H, 7.03%. %. Found: C, 77.19; H, 6.87%.

Table 4, row 12

6-Ethyl-4-methyl-2H-chromen-2-one (12): Yellow solid. m.p.: 159–160 °C. IR (KBr) ν_{max} (cm^{-1}): 1660 (ester C=O stretch), 1580 (C−C=C stretch). ^{1}H-NMR (DMSO-d6) δ: 1.82 (t, J = 7.2, 3H, CH_3), 2.32 (s, 3H, CH_3), 3.64 (q, J = 7.2, 2H, CH_2), 5.90 (m, 1H), 7.11 (d, J = 8.5, 1H), 7.34 (dd, J = 8.5, 2.2, 1H), 7.40 (s (br), 1H); ^{13}C-NMR (DMSO-d6) δ: 16.7, 18.9, 22.3, 115.2, 118.5, 123.4, 124.9, 130.7, 135.2, 155.4, 161.3. MS (m/z): 188 (M+). Anal. Calcd for $C_{12}H_{12}O_2$: C, 76.57; H, 6.43%. Found: C, 77.28; H, 6.39%.

Table 4, row 13

6-Isopropyl-4-methyl-2H-chromen-2-one (13): Yellow solid; m.p.: 167–169 °C. IR (KBr) ν_{max} (cm^{-1}): 1657 (ester C=O stretch), 1580 (C−C=C stretch). ^{1}H-NMR (DMSO-d6) δ: 1.63 (d, J = 6.5, 1H, CH), 2.42 (s, 3H, CH_3), 2.93 (q, J = 6.5, 6H, $2CH_3$), 5.87 (m, 1H), 7.13 (d, J = 8.3, 1H), 7.32 (dd, J = 8.3, 2.3, 1H), 7.42 (s (br), 1H); ^{13}C-NMR (DMSO-d6) δ: 14.5, 15.2, 18.2, 24.7, 116.3, 119.0, 122.6, 126.4, 133.2, 137.6, 157.4, 163.3. MS (m/z): 202 (M+). Anal. Calcd for $C_{13}H_{14}O_2$: C, 77.20; H, 6.98%. Found: C, 76.56; H, 6.69%.

Results and Discussion

Preparation of nanosilica using sol-gel method

Sol-gel method is one of the several methods that can be used to synthesize various nanoparticles. This method starts with the formation of a homogeneous cell from the starting material and then, the cell is converted into a gel through chemical stimulation. Then, the solvent is removed from the gel structure and dried using one of the common methods. Depending on the drying method, the product will have different properties. Depending on the application that the gel is synthesized for, the solvent deposition can be different. Different types of dry gels have a variety of applications in coating surfaces, insulation of buildings, special cloths, etc. In the meantime, if the gel is powdered with special mills, particles in the nanoscale can be achieved.

The sol-gel process is a bottom-up synthesis method. In this process, the resulting product contains a number of irreversible chemical reactions. In fact, these reactions result in formation of the primary homogeneous soluble molecules called cells, which turn to an unlimited, heavy, and three-dimensional polymeric molecule called a gel. The hydrolytic reaction, the condensation reaction which follows the hydrolytic reaction, and the final product obtained are summarized in Figure 1.

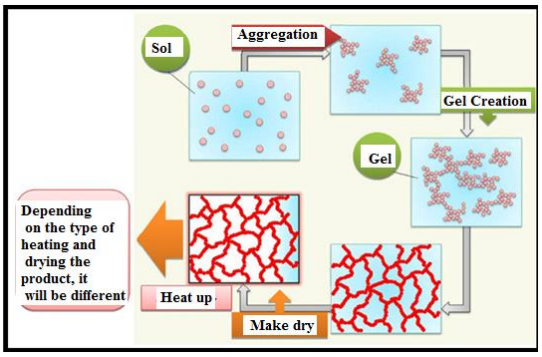

Figure 1. Sol-gel and hydrolysis process

In the sol-gel process, converting a cell to the gel state is often performed by changing the pH or solution concentration. The main reasons for using the cell-gel process are production of a high-purity product, distribution of the fine particle size, and achievement of uniform nanostructures at low temperatures. The sol-gel method is often used to prepare nano-metal oxides.

In a scientific resource, synthetic nanosilica has been synthesized using the mineral compound of sodium silicate, halosilane compounds, and organo-silanes such as tetraethyl ortho-silane or tetraethoxysilane (TEOS) with the formula of $Si(OC_2H_5)_4$ and tetramethoxysilane (TMOS) [21].

Two classes of techniques have been developed for the formation of silica nanoparticles: sol-gel method and micro-emulsion method. The pathway of micro-emulsion is the same as the sol-gel pathway. In these systems, surfactants are added to the nanoparticle cell system. Surfactants create a coating on nanoparticles in a way that the internal core contains nanoparticles and the surface layer of the surfactant. The micro-emulsion pathway is really appropriate for preparation of particles with a small diameter, narrow size distribution, and high surface area [22-23].

Importance of using hydrogen sulfate to be stabilized on nanoparticles

Several reactions such as Friedel-Craft, sterification, aldol condensation, oxidation, etc. are carried out under acidic conditions. In these types of reactions, different acids are used for acidification, including mineral acids such as HCl, H_3PO_4, and H_2SO_4, lewis acids such as $ALCl_3$ and $FeCl_3$, and organic-metal compounds. In the meantime, their application is limited by problems such as lack of easy access, slipping, difficult transportation conditions, high corrosion, and toxicity of most of the minerals.

Therefore, chemists have sought to eliminate the problems of using them by introducing and using compounds that can be a successor to the previous cases in addition to having high acidity. In recent years, the use of metal hydrogen sulfates such as Al, Na, K, Mg, and Fe has been considerably expanded. Hydrogen sulfates are solid compounds, so working with them is easier. These compounds with proper acidity appeared strongly in most reactions, so that in most of the cases, the reactions are performed with very good to excellent efficiency and less byproducts; also, product retrieval is performed through a simple method. In some cases, in the absence of a solvent, it is possible to produce products whose efficiency is even higher than the solution phase and this method has no environmental problems resulted from using the solvent [24-28].

By passing from microscale to nanoscale, some physical and chemical properties are observed, two of the most important of which are: an increase in the ratio of the surface area to volume and the entry of particle size into the domain of quantum effects. Increasing the surface greatly increases the reactivity of nanoscale materials because the number of molecules or atoms in the bulk is very high, so that these particles tend to aggregate. In some cases, in order to maintain the desired properties of the

nanomaterials to prevent further reactions, a stabilizer should be added to resist against erosion, fatigue, and corrosion.

By using these materials in production of nanocomposites, stronger chemical bonds can be formed between the support and particles and their strength is increased. Consequently, transformation of composite into nanocomposite increases strength. On the other hand, increasing the surface of the particles reduces the surface pressure and leads to a change in the distance between the particles and the distance between the atoms of the particles.

Nanomaterial components can have the combined properties of both of the components and act better because of interaction between the support surface and the filler particles. Among these materials, layer silicates and clay particles have been interesting and were studied more because of their availability and harmlessness in the environment. In the meantime, silica has been more interesting due to its smooth structure, high surface area, functionality, and having nanoscale pores [63]. By adding particles, the nanoscale properties of the material will improve when:

(1) there is enough interaction between nanoparticles and the support.

(2) there is proper dispersion of particles between the support.

Due to high importance of synthesizing coumarin derivatives (2-H-chromen-2-one) as a drug, whose biological properties have been mentioned, and since the methods of improving preparation of this compound are being updated, we tried to synthesize some of the 2H-chromium-2-one derivatives in the presence of the catalyst of hydrogen sulfate stabilized on nanosilica particles. This method has a lot of advantages, including environmental compatibility, short reaction time, easy recovery and reuse of the catalyst, and high product efficiency.

The basis of this research is studying the speed and efficiency of the Pechmann condensation reaction to synthesize some of the coumarin derivatives in the presence of sodium hydrogen sulfate catalyst stabilized with nanosilica.

In order to obtain a correct ratio of the catalyst, solvent, and optimal conditions, the resorcinol and ethyl acetoacetate reactions were investigated. In order to optimize the catalyst, various amounts of sodium hydrogen sulfate and nanosilica were mixed and used in successive experiments. The best result was obtained when 0.1 g of nanosilica was mixed with 0.2 g of sodium hydrogen sulfate (Table 1).

Table 1. Optimization of the amount of catalyst components

The amount in gram	Catalyst components
0.1 gr	SiO_2(nano)
0.2 gr	$NaHSO_4$

The size of the nanosilica particle prepared by the sol-gel method was measured by the SEM device and its size was 19.53 nm (Figure 2). After stabilizing sodium hydrogen sulfate on silica nanoparticles, the particle size increased to 27.34 nm, indicating the correct stabilization of sodium hydrogen sulfate on nanosilica (Figure 3).

Figure 2. The SEM image of nanosilica particles

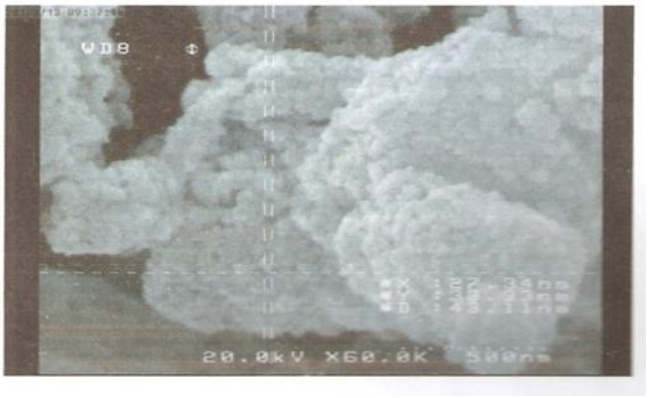

Figure3. The SEM image of nanosilica particles supported by sodium hydrogen sulfate

The general method for synthesizing coumarin derivatives through Pechmann method is as follows (Figure 4).

To select the appropriate solvent for this reaction, several solvents were tested in the presence of 0.3 g of catalyst. Acetonitrile was selected as the optimum solvent with 85% efficiency at 25 min (Table 2).

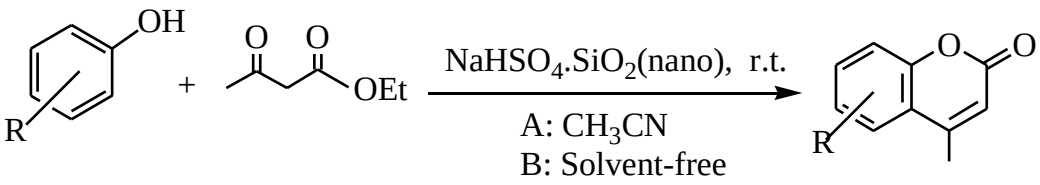

Figure 4. Synthesis of Coumarin Derivatives by Pechmann Method in the Presence of Sodium Hydrogen Sulphate Stabilizad on Nanosilica in Solvent and Solvent-free Conditions

Table2. The optimal condition for solvent

No	Solvent	Reaction Condition	Time (min)	Recovery (%)
1	Dichloromethane	Room Temperature	120	45
2	Acetonitrile	Room Temperature	25	85
3	Ethanol	Room Temperature	45	67
4	Acetone	Room Temperature	-	-
5	DMF	Room Temperature	240	22

The sign (-) indicates that the reaction did not occur

After choosing the solvent, it is time to select the optimal amount of catalyst. Different amounts of catalysts were investigated in an optimum solvent. The reaction efficiency reached its highest value by using 0.05 gr of the catalyst. Any increase or decrease in the optimum amount of catalyst did not have an ascending effect on the reaction speed (Table 3).

Table 3. The optimal conditions for the amount of catalyst in the acetonitrile solvent

No	Reaction Condition	Amount of catalyst (mole percent)	Time (min)	Recovery (%)
1	Room Temperature	0.01	65	85
2	Room Temperature	0.03	35	80
3	Room Temperature	0.05	25	90
4	Room Temperature	0.001	60	45
5	Room Temperature	0.003	120	52

After optimizing the conditions, the reaction of various derivatives of coumarin in optimal conditions was investigated and the results are shown in Table 4. According to the results, this method can be performed with a good to excellent yield for all of the phenolic compounds with electron-donating and electron-accepting groups and even with two or three groups of hydroxyl, and it seems that the above mentioned groups do not considerably affect reaction efficiency. These results show that the effect of a catalyst with nano-substrate and wide surface accelerates preparation of coumarins in a way that the effect of accepting and donating the substitutions is insignificant compared to it.

In Table 5, the efficiency of the method proposed for synthesizing coumarin derivatives has been compared with other published articles. According to table 5, sodium hydrogen sulfate catalyst stabilized with nanosilica provides better time and efficiency at ambient temperature for performing this reaction (Table 5, rows 5 and 6), while other catalysts offer a long time, low yield, and high temperatures (Table 5, rows 1 to 4).

Regarding the mechanism presented in Fig. 5, it seems that the hydrogen sulfate anion stabilized on a vast surface of the nanosilica has a high yield and can simultaneously play double roles. First, it accelerates the tautomeric balance of the enole to ketone and second, it causes adsorption of the electron in the oxygen anion of the carbonyl group in this stage. Then, the ring is closed by attacking of the electron pair of oxygen to the carbonyl group and removing a water molecule, and in

the final step, the final product will be achieved by recovering the catalyst.

Table 4. The results obtained for synthesis of coumarins in the presence of sodium hydrogen sulfate stabilized with nanosilica

No	Raw Materials	Product	With Solvent		Solvent-free		Melting Point	
			Time (min)	Yield[A] (Percent)	Time (min)	Yield[B] (Percent)	Observed	Reported
1	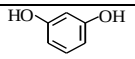	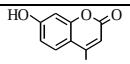	25	85	10	85	187-188	183-189 [29]
2	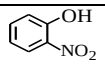	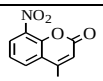	15	80	8	90	183-184	183-185 [29]
3	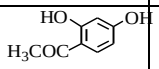	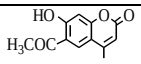	30	85	20	80	165-166	164-165
4	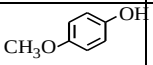	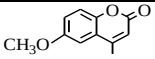	35	85	10	85	169-170	165 [29]
5	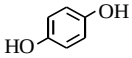	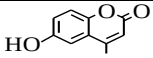	20	90	8	90	246-247	243-247 [29]
6			35	88	15	90	140-151	154-155 [29]
7	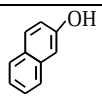	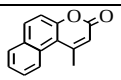	20	85	10	90	181-182	180-181 [29]
8		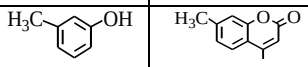	30	85	15	85	130-132	131-133 [29]
9	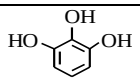	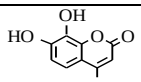	40	80	25	85	237-238	236-239 [30]
10	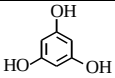	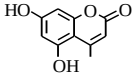	30	95	10	95	280-282	283-284 [29]
11		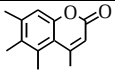	13	80	8	80	164-165	165-165 [29]
12		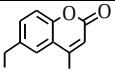	10	85	5	85	159-160	160-162 [29]
13		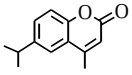	10	80	10	80	167-169	168-170 [29]

A: reaction conditions: Phenol (1 mmol), ethyl acetate (1 mmol), 0.05 gr of catalyst, 3 ml of acetonitrile (under solvent conditions), at ambient temperature; The reaction is carried out in the absence of solvent with the same molar conditions. B: Separation Recovery

Table 5. Comparison of this method with other reported methods for synthesis of coumarins using resorcinol

No	Catalyst	Amount of catalyst (mole percent)	Condition	Time (min)	Recovery (%)	References
1	Oxalic acid	10	Silvent-free/80°C	30	95	[31]
2	Nanoreactors	7	Silvent-free/130°C	120	67	[31]
3	FeF_3	0.05 gr	Ethanol/Reflux	1.5	93	[30]
4	PFPAT	10	Toluene/110°C	180	90	[31]
5	$NaHSO_4$-SiO_2	3	Acetonitrile/Reflx	60	95	[32]
6	NP-HSO_4	0.05 gr	Acetonitrile/Room temperature	22	85	Present study
7	NP-HSO_4	0.05 gr	Solvent-free/Room temperature	10	85	Present study

Conclusion

Due to the high importance of synthesis of coumarin derivatives (2-H- chromen-2- one) as a drug, whose biological properties were mentioned, and since the preparation methods of this compound are improving continuously, we sought to synthesize some of the 2-H-chromen-2- one derivatives in the presence of a hydrogen sulfate catalyzer immobilized on nanosilica particles. This method has several advantages including environmental compatibility, short reaction time, easy recovery, catalyst reuseability (at least 3 times), and high yield.

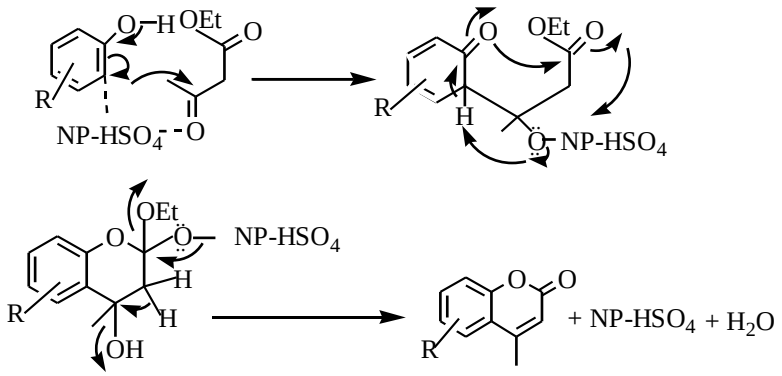

Figure 5. |Preparation mechanism of coumarins using sodium hydrogen sulfate reagent stabilized on nanosilica (NP-HSO_4)

Acknowledgment:

The authors of the article are sincerely grateful to Vice-Chancellor of Research and Technology of Azarbaijan Shahid Madani University for the financial support.

References

[1] Guibourt. N. J. B. G, Histoire Abrégée des Droques Simples (Abridged History of Simple Drugs), Volume 2. Paris, L. Colas. 1820, 160.

[2] Guibourt. N. J. B. G, Histoire Naturelle des Drogues Simples, 6th ed. Paris, J. B, Baillière et fils. 1869, 377.

[3] Kennedy. R.O, Thornes. R. D, wiley and Sons, Chichester, 1997.

[4] Mitsuy. M, Suzuki. T, Koyama. T, Appl. Phys. Lett. 2000, 77, 3272.

[5] Heveling. J, Journal of Chemical Education, 2012, 1530.

[6] Tabrizian. E, Amoozadeh. A, Journal of applied chemistry, 2014, 2, 9, 23.

[7] Koukabi. N, Otokesh. S, Amoozadeh. A, Kolvari. E, Journal of applied chemistry, 2014, 2, 9, 31.

[8] Kolvari. E, Amoozadeh. A, Azhari. S, Otokesh. S, Journal of applied chemistry, 2014, 2, 9, 79.

[9] Zolfigol. M. A, Tetrahedron, 2001, 57, 9509.

[10] Nicolaou. K. C, Pfefferkorn. J. A, Roecker. A. J, Cao. G. Q, Barluenga. S, Mitchell. H. J, J. Am. Chem. Soc. 2000, 122, 9939.

[11] Kazuo. M, Kazuya. O, Hironobu. H, Mukai. K, Okabe. K, Hososе. H, J. Org. Chem. 1989, 54, 557.

[12] Kostova. I, Curr. Med. Chem. 2005, 5, 29.

[13] Yourick. J. J, Bronaugh. R. L, J. Appl. Toxicol. 1997, 17, 153.

[14] O'Kennedy. R, Thornes. R. D, John Wiley &Sons, New York, 1997.

[15] Nielson. B. E, Heywood in the Biology and Chemistry of the Umbelliferon, Academic Press, London, 1971.

[16] Murray. R. D. H, Mendez. J, Brown. S. A, Chemistry and Biochemistry, John Wiely & Sons, New York, 1982.

[17] Yamazaki. H, Tanaka. M. T, Shimada. J, Chromatogr, B, 1999, 13.

[18] Izquierdo, M. E. F, Granados. J. Q, Mir. V. M, Martinez. M. C. L, Food Chem. 2000, 70, 25.

[19] Trenor. S. R, Shultz. A. R, Love. B. J, Long. T. E, Chem. Rev. 2004, 104, 3059.

[20] Park. S. W, Seo. B. S, Kim. E. H, Kim. D. H, Paeng. K. J, J. Forensic Sci. 1996, 41, 685.

[21] Abri. A, Ranjdar. S, J. Chin. Chem. Soc., 2014, 61, 929.

[22] Abri. A, Assadi. M. G, Pourreza. S, J. Chin. Chem. Soc., 2014, 61, 929.

[23] Hatay. I, Gup. R, Ersoz. M, J. Hazard. Mater., 2008, 150, 546.

[24] Entezari. M. H, Kruus. P, Otson. R, Ultrason. Sonochem., 1996, 4, 49.

[25] Ramesh. C, Mahender. G, Ravindranath. N, Biswanath Das. N, J. Tetrehedron Letters., 2003, 44, 1465.

[26] Fulchand. C, Balaji. M, Jagdish. B, Milind. U, Madhav. W, Murlidhar. S, Naryn. S, Bull. Catal. Soc. Ind., 2008, 7, 41.

[27] Gopalakrishnan. M, Sureshkumar. P, Kanagarajan. V, Thanusu. J, Thirunavukkarasu. S, J. Korean. Chem. Society., 2007, 51, 346.

[28] Biswanath. D, Anjoy. M, Banerjee. J, J. Tetrahedron. Lett., 2006, 47, 7619.

[29] Rostamizadeh. S, Shadjou. N, Amanl. S, Balalaie. A. M, J. Chinese. Chem. Lett., 2008, 19, 1151.

[30] Amoozadeh. A, Ahmadzadeh. M, Kolvari. E, J. Chem. 2013, 1, 6.

[31] Vahabi. V, Hatamjafari. F, Molecules, 2014, 19, 13093.

[32] Vahdat. S. M, J. Appl. Chem. 2012, 7, 57.

[33] Das. B, Venkateswarlu. K, Mahender. G, Holla. H, J. Chem. Res. (S) 2004, 83.

Communications In Catalysis
Vol. 1, No. 2, 2024, pp.35-56
DOI: 10.22049/CIC.2018.26341.1022

Azarbaijan Shahid Madani University

Tetracycline and Doxycycline photocatalytic degradation by Nano α-Fe_2O_3/12-tungstosilicic acid prepared through forced hydrolysis and reflux condensation

Majid Saghi, Kazem Mahanpoor*

Department of Chemistry, Arak Branch, Islamic Azad University, Arak, Iran , P.O. Box 38135/567,.

* Corresponding Author. Tel: +988633412222.

E-mail: address: k-mahanpoor@iau-arak.ac.ir

Received: 2024-11-20, Revised: 2024-12-03, Accepted: 2024-12-12

Abstract

In the research, spherical α-Fe_2O_3 nanoparticles (NPs) were synthesized and supported on the surface of 12-tungstosilicic acid (12-TSA.7H_2O) using forced hydrolysis and reflux condensation (FHRC) method. Photocatalytic activity of pure and supported α-Fe_2O_3 NPs (α-Fe_2O_3/2-TSA.7H_2O) for Tetracycline (TC) and Doxycycline (DC) degradation was investigated using UV/H_2O_2 process. The products were characterized by FTIR, SEM/EDX, BET surface area and XRD. The experiments were designed considering four variables including pH, the initial concentration of pollutant, catalyst concentration and H_2O_2 concentration at two-levels and three central point's using full factorial experimental design. The results indicated that supporting α-Fe_2O_3 NPs caused to improve the filtration, recovery and photocatalytic activity of NPs. Under optimal conditions, 88.44% TC and 87.67% DC were degraded following 50 and 120 min, respectively. The results indicated that reactions follows first-order kinetic and rate coefficient for TC and DC degradation reactions equals to 0.0178 and 0.0074 min^{-1}, respectively.

Keywords: Tetracycline; Doxycycline; Full factorial; α-Fe_2O_3; α-Keggin.

Introduction

The numerous reports have stated the existence of antibiotics such as TC and DC in water resources such as urban and industrial wastewaters, drinking waters, surface waters and ground waters [1-6]. It is common to use photocatalytic processes for degradation of pharmaceutical pollutants but using effective, economically-reasonable and recoverable catalysts is highly important. In some photocatalytic processes, it is necessary to use supported catalysts. The supported catalysts comprise two major segments: catalyst and catalyst support. Catalyst is commonly made up of active and effective segment of these composites but there are numerous cases where catalyst support is active too [7]. Using the supported catalysts could be due to different causes but enhancing the catalytic activity and their more convenient recovery are two common purposes for affixing catalyst on the surface of catalyst support. Various organic, inorganic or organic/inorganic materials could be used as catalyst support [8, 9]. Selecting the suitable catalyst support depends to some factors such as conditions governing the process, chemical and physical properties of the desirable catalyst and catalyst support, etc. Polyoxometalates (POMs) are a class of inorganic compounds as multi-core clusters which could be used as catalyst support [10]. POMs are divided into two categories of isopolyanions (IPAs) and heteropolyanions (HPAs). In molecular structure of IPAs, there are only oxygen and metal atoms, whereas HPAs have at least one hetero atom (Si, P, As, B, etc.) in addition to metal and oxygen [11]. Thermodynamically, HPAs have stable arrangements and maintain their crystal structure in aqueous and non-aqueous solutions; therefore they could be used as catalyst support under different conditions. This class of materials has various applications in catalysis [12], analytical chemistry [13], medicinal chemistry (anti-tumor, anti-cancer, anti-bacteria, anti-microbial and anti-clotting) [14-16], radioactive materials [17] and gas absorbents [18]. HPAs have different structures of which α-, β-, γ-, δ- and ε-Keggin, Wells–Dawson, Preysler, Strandberg and Anderson–Evans are served as critical types. 12-TSA is a HPA with formula $H_4SiW_{12}O_{40}$ and α-Keggin structure (see Figure 1). The central Si heteroatom is surrounded by a tetrahedron whose oxygen vertices are each linked to one of the four W_3O_{13} sets. Each W_3O_{13} consists of three W_3O_6 octahedrals linked in a triangular arrangement by sharing edges and the four W_3O_{13} are linked together by sharing corners [19].

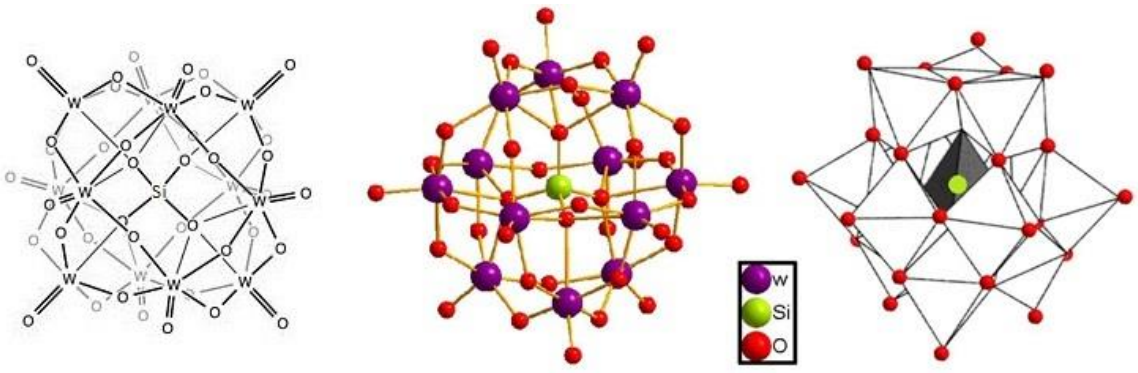

Figure. 1 α-Keggin structure of $[SiW_{12}O_{40}]^{4-}$.

Using nanocatalysts (Those catalysts whose particles are 1-100 nm) could be more effective in photocatalytic processes. Metal oxide NPs i.e., iron oxides, have a special position in the science and technologies because of having wide applications and unique properties [20-22]. α-Fe_2O_3 (hematite) which is the most common form of iron oxides, has the rhombohedral structure and it is an attractive compound because of its applications in data storage, gas sensor, magnets materials, pigment, catalysis and photocatalysis [23-28]. Various techniques including co-precipitation, sol-gel, thermal decomposition, Micelle synthesis, sonochemical synthesis, hydrothermal synthesis and FHRC have been utilized to synthesize monodisperse α-Fe_2O_3 NPs [29-35]. Since chemical degradation and removing the pollutants existed in aqueous medium is one of most critical use of photocatalytic processes, so using supported catalysts could be very helpful because in addition to increase the performance of degradation, it provides convenient recovery of catalyst from polluted solution and its reuse. In order to optimize a process like the photocatalytic degradation process, it is essential to study all factors influencing the process. But studying the effects of individual factors on the process is difficult and time-consuming, especially if these factors are not independent and they affect each other. Employing experimental design could eliminate these problems because the interaction effects of different factors could be attained using design of experiments (DoEs) only. Full factorial is an appropriate method for DoEs because it could reduce the total number of experiments as well as optimize the process by optimizing all the affecting factors collectively, at a time [36]. The design could determine the effect of each factor on the response as well as how this effect varies with the change in level of other factors. In the paper, spherical α-Fe_2O_3 nanoparticles were synthesized and supported on the surface of 12-TSA using FHRC method. The catalyst of α-Fe_2O_3/12-TSA was used in order to remove TC and DC antibiotics under UV/H_2O_2 process. The molecular structures of TC and DC are shown in Figure 2.

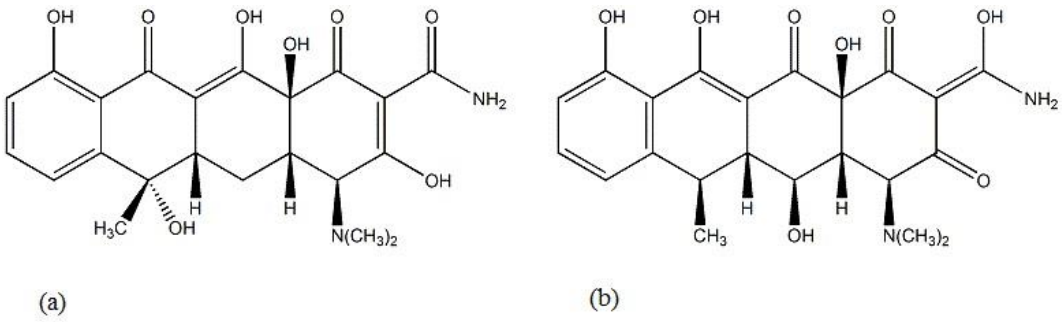

Figure 2. TC (a) and DC (b) Molecular structures.

Experimental

Material and Apparatuses

All chemicals including sodium tungstate dihydrate, sodium silicate, diethyl ether, iron (III) chloride hexahydrate, urea, hydrogen peroxide (30%), hydrochloric acid (37%), sulfuric acid (96%), sodium hydroxide and ethanol were purchased from Merck. Also, the required TC and DC were purchased from Razak and Iran Daru pharmaceutical laboratories, respectively. Deionized water was used throughout the experiments. The Fourier Transform Infra-Red (FTIR) spectra of products were recorded on a Perkin-Elmer spectrophotometer (Spectrum Two, model) in the range of 450-4000 cm^{-1}. The shape, morphology and elemental analysis of 12-TSA.7H_2O and α-Fe_2O_3/12-TSA.7H_2O surfaces were examined using a Philips XL-30 Scanning Electron Microscope/Energy Dispersive X-ray spectroscopy (SEM/EDX). The X-Ray Diffraction (XRD) analysis of the samples was done using a DX27-mini diffractometer and BET surface area of materials was determined by N_2 adsorption–desorption method at 77 K, measured using a BELSORP-mini II instrument. Also, all Ultraviolet/Visible (UV/Vis) absorption spectra were obtained using an Agilent 8453 spectrophotometer.

Synthesis of α-Fe_2O_3 NPs

The synthesis of α-Fe_2O_3 NPs was carried out according to Bharathi et al [35]. Firstly, 100 ml iron (III) chloride hexahydrate 0.25 M was poured into a flat-bottom flask. When iron solution was agitated, it was added drop by drop to it 100 ml urea 1 M. The obtained mixture was stirred for 30 min and then placed under the reflex at 90-95 ^oC for 12 h. Then, the precipitate after separation was washed with 100 ml deionized water because unreacted ions will be completely removed. The washed precipitate was dried at 70 ^oC for 2 h. Finally, this solid remained at 300 ℃ for 1 h, hence the iron hydroxide particles will transform to iron oxide.

Synthesis of 12-TSA.7H_2O

12-TSA.7H_2O was synthesized according to literature procedure [37]. Firstly, 15 g sodium tungstate dihydrate was dissolved in 30 ml deionized water and then 1.16 g sodium silicate solution with a density of 1.375 g/ml was added to it. The resulted mixture was heated up to about boiling point, and while it was stirred, 10 ml concentrated HCl was added to it during 30 min, smoothly. Then, the solution was naturally cooled down to room temperature and slight precipitate formed (silicic acid) in it was filtered. Again, 5 ml concentrated HCl was added to the solution and was transferred to separatory funnel after cooling it again down to room temperature. Then, 12 ml diethyl ether was added to it and well shaken. Therefore, three layers were formed inside separatory funnel, middle layer of which was yellow-colored. Bottom layer which was oily ether was separated and transferred into a beaker. In order to further extract, separatory funnel was further shaken again and the bottom layer was once more separated and transferred into the beaker. The extraction process

was done so much that the yellow color of middle layer was fully faded. The extracted ether complex which was inside the beaker was transferred to another separatory funnel and then 16 ml HCl 25% v/v was added to it. Next, 4 ml diethyl ether was added to it, subsequently. The contents inside separatory funnel were shaken and bottom layer (ether) was transferred to the evaporating dish after separating. Evaporating dish was exposed to air and remained motionless to evaporate the solvent and form the 12-TSA.$7H_2O$ crystals. Finally, 12-TSA.$7H_2O$ formed crystals were placed at 70 ^oC for 2 h until it was completely dried. The chemical reaction occurred in the process of 12-TSA.$7H_2O$ synthesis has been shown in (1) [37].

(1) $12\ Na_2WO_4 + Na_2SiO_3 + 26\ HCl \rightarrow H_4SiW_{12}O_{40}.xH_2O + 26\ NaCl + 11\ H_2O$

Preparation of α-Fe_2O_3/12-TSA.$7H_2O$ (FHRC method)

Firstly, 50 ml iron (III) chloride hexahydrate 0.25 M was poured into a beaker. While it was agitated by stirrer, 3.5 g 12-TSA.$7H_2O$ was gently added to it. The obtained mixture was stirred for 4-5 h. The solid accumulated at bottom of beaker was separated and transferred into one flat-bottom flask and the same 10 ml solution inside beaker was added to it. When mixture was being stirred, 50 ml urea 1 M was gradually added to it. The mixture was placed under reflux at 90-95 ^oC for 12 h. Then, the precipitate resulted after separation was washed with 100 ml ethanol/deionized water 1:1 solution because unreacted ions were completely removed. The washed precipitate was dried at 80 ^oC for 2 h. In order to calcination, the obtained solid was kept at 300 ^oC for 1 h.

Experimental design

The photocatalytic efficiency of products on the TC and DC degradation was investigated using full factorial experimental design. The experiments were designed considering four variables including pH, the initial concentration of pollutant, catalyst concentration and H_2O_2 concentration at two-levels and three central points. Experimental range and levels of variables are shown in Table 1. Also, 19 experiments related to this factorial have been listed in Table 2.

Table 1. Experimental range and levels of the variables

Variables	Range and levels					
	For TC pollutant			For DC pollutant		
	–1	0	+1	–1	0	+1
pH	4	6	8	4	6	8
Initial Con. of pollutant (ppm)	30	50	70	80	100	120
Catalyst Con. (ppm)	50	100	150	100	125	150
H_2O_2 Con. (ppm)	0.1	0.3	0.5	1	1.5	2

Table 2. Experimental conditions for photocatalytic process

Exp. No.	Variable			
	pH	Initial Con. of pollutant (ppm)	Catalyst Con. (ppm)	H_2O_2 Con. (ppm)
1	–1	–1	–1	–1
2	+1	–1	+1	+1
3	–1	–1	+1	–1
4	–1	+1	+1	–1
5	+1	+1	+1	–1
6	0	0	0	0
7	+1	–1	+1	–1
8	–1	+1	–1	+1
9	+1	–1	–1	–1
10	+1	+1	+1	+1
11	–1	+1	–1	–1
12	+1	–1	–1	+1
13	+1	+1	–1	–1
14	–1	+1	+1	+1
15	+1	+1	–1	+1
16	0	0	0	0
17	–1	–1	+1	+1
18	0	0	0	0
19	–1	–1	–1	+1

General procedure

Figure 3 shows one schematic diagram of photocatalytic reactor used in the work. An MDF box was designed inside which a circular Pyrex reactor was placed. On the upper section of the box, three mercury lamps were built-in as UV light sources. The radiation is generated almost exclusively at 254 nm. The liquid inside the reactor was agitated by magnetic stirrer and the air inside the box was conditioned by a fan. In order to carry out each experiment, firstly 250 ml polluted solution was made as specified concentration and poured inside the reactor. Then, at related pH, the specified amount of catalyst and H_2O_2 were added to the solution inside the reactor. In all experiments, pH adjustment was done via minimum use of H_2SO_4 and NaOH. Then, stirrer and UV lamps were immediately turned on to initiate the process. In order to fully separate the catalyst from solution, the samples were centrifuged for 3 min with 3500 rpm speed. The concentrations of TC and DC in the samples were determined using a UV/Vis spectrophotometer at λ_{max}=357 and 347 nm, respectively. The percentage of pollutant decomposition (x%) as a function of time is given by

$$x\% = \frac{C_0 - C}{C_0} \times 100 \quad (2)$$

Where C_0 and C are the concentration of pollutant (ppm) at t=0 and t, respectively.

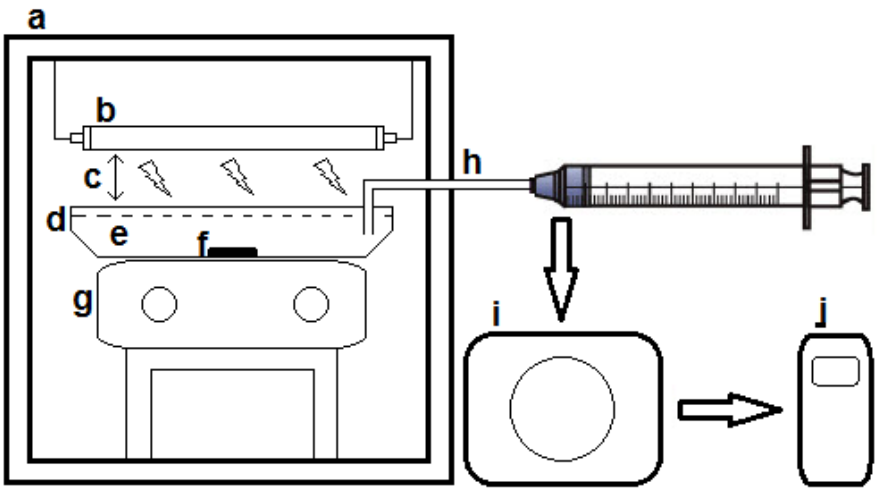

Figure 3. Schematic diagram of photo reactor.
(a) MDF box, 50×50×50 cm; (b) Mercury lamps, Philips 15W; (c) The distance between surface of polluted solution and lamps, 5 cm; (d) Reactor, 300 ml capacity; (e) The polluted solution, 250 ml; (f) Magnet; (g) Magnetic stirrer; (h) Sampling port; (i) Centrifuge, 3 min; (j) UV/Vis spectrophotometer.

Result and Discussions

Characterization of 12-TSA.7H_2O

SEM image of 12-TSA.7H_2O is shown in Figure 4. Suitable area and the pores existed on the surface of this catalyst support provide an appropriate conditions to support α-Fe_2O_3 NPs. IR is a suitable method for the structural characterization of HPAs [11]. FTIR spectrum of the synthesized 12-TSA.7H_2O has been shown in Figure 5a. There are four kinds of oxygen atoms in 12-TSA.7H_2O structure, 4 Si-O_a in which one oxygen atom connects to Si, 12 W-O_b-W oxygen bridges (corner-sharing oxygen-bridge between different W_3O_{13} groups), 12 W-O_c-W oxygen bridges (edge-sharing oxygen-bridge within W_3O_{13} groups) and 12 W=O_d terminal oxygen atoms. The symmetric and asymmetric stretching of the different kinds of W-O bonds are observed in the following spectral regions: Si-O_a bonds (1020 cm^{-1}), W=O_d bonds (1000-960 cm^{-1}), W-O_b-W bridges (890-850 cm^{-1}), W-O_c-W bridges (800-760 cm^{-1}) [38]. In Table 3, vibrational frequencies of the synthesized 12-TSA.7H_2O and equivalent values reported in previous studies [38, 39] have been listed. Comparing the vibrational frequencies reveals that 12-TSA.7H_2O has been well synthesized. XRD is one of the most important characterization tools used in solid state chemistry and materials science. Figure 6a shows the XRD pattern of 12-TSA.7H_2O. This pattern indicates that the characteristic peaks corresponded to the 12-TSA were well appeared and it means that the synthesized 12-TSA.7H_2O crystals were well formed [39].

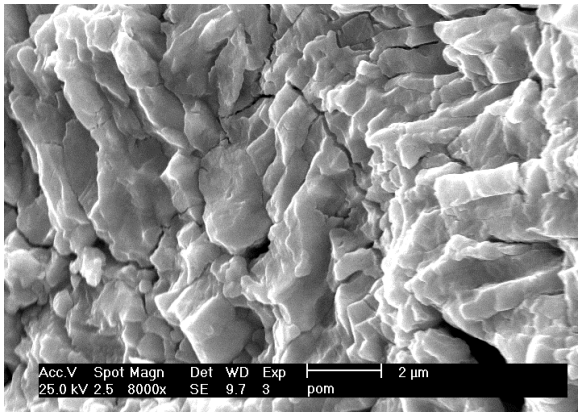

Figure 4. SEM image of the synthesized 12-TSA.7H_2O.

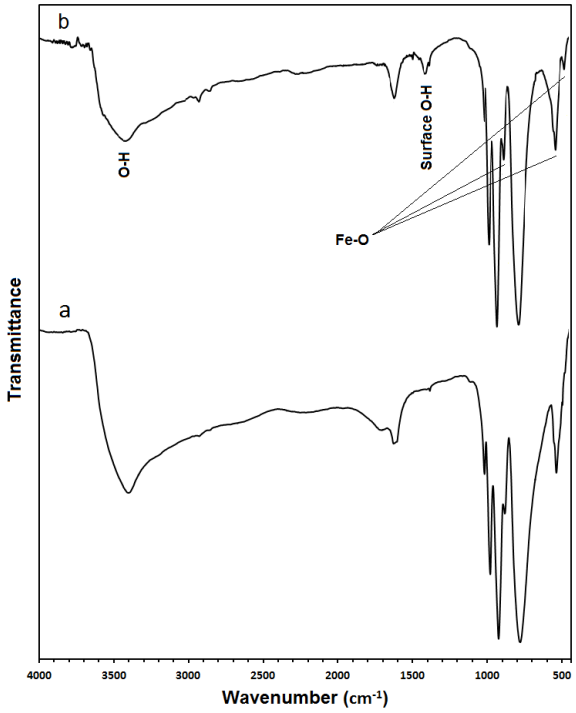

Figure 5. FTIR spectra of the synthesized 12-TSA.7H_2O (a) and α-Fe_2O_3/12-TSA.7H_2O (b).

Table 3. Vibrational frequencies of the synthesized 12-TSA.7H_2O and equivalent values reported in previous reports

Number	The synthesized 12-TSA.7H_2O		[38, 39]
	Wavenumber (cm^{-1})	Transmittance %	
1	1019.04	13.29	1020 (weak)
2	980.68	8.81	981 (sharp)
3	924.31	5.92	928 (very sharp)
4	882.63	11.52	880 (medium)
5	780.28	5.77	785 (very sharp)
6	537.41	13.35	540 (medium)

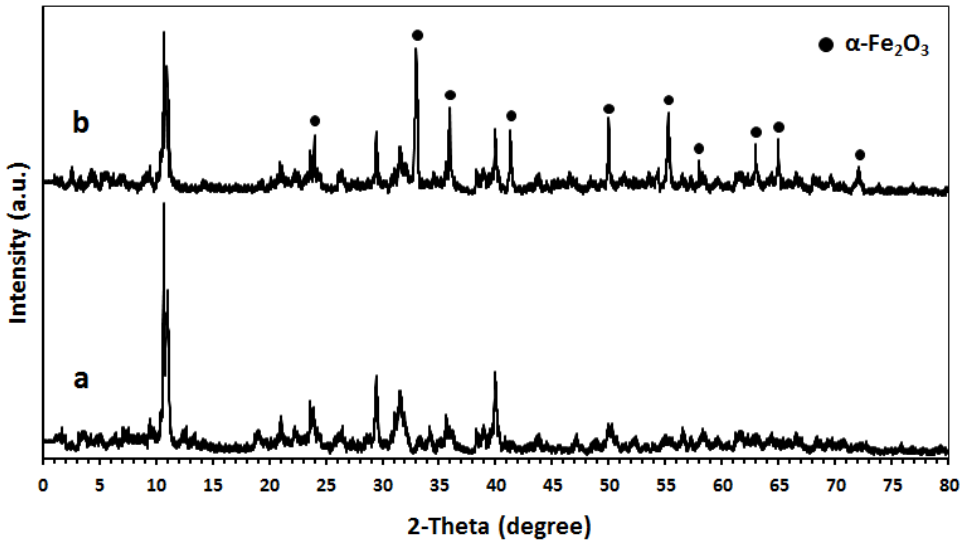

Figure 6. X-ray diffractogram of the synthesized 12-TSA.7H_2O (a) and α-Fe_2O_3/12-TSA.7H_2O (b).

Characterization of α-Fe_2O_3/12-TSA.7H_2O

Figure 7 shows SEM/EDX results of α-Fe_2O_3/12-TSA.7H_2O. SEM image indicate that α-Fe_2O_3 particles were spherically supported on the surface of 12-TSA.7H_2O. In the EDX spectrum, peaks of three main elements in α-Fe_2O_3/12-TSA.7H_2O namely Si, W and Fe were appeared and named. Au peaks in the EDX spectrum is due to samples coverage's with a thin layer of gold before SEM/EDX analysis. Generally, the result of EDX indicated that α-Fe_2O_3 particles were supported on the surface of 12-TSA.7H_2O. In Figure 5b, FTIR spectra of α-Fe_2O_3/12-TSA.7H_2O have been shown. It is clear that absorption peaks of 12-TSA.7H_2O have appeared without considerable change in the wavenumbers (only their intensities have been slightly changed). It means that 12-TSA.7H_2O was stable and it had not been changed chemically during preparing α-Fe_2O_3/12-TSA.7H_2O. Also, absorption peaks of α-Fe_2O_3 have well appeared and are in agreement with results of Bharathi et al [35]. These absorption peaks which are related to stretching and bending modes of OH and Fe-O binding in FeOOH, in some cases overlapped with absorption peaks of 12-TSA.7H_2O. In Fig. 6b, XRD pattern of α-Fe_2O_3/12-TSA.7H_2O have been illustrated. In the pattern, characteristic peaks of 12-TSA.7H_2O have well appeared which indicates that 12-TSA.7H_2O was stable during the supporting process. Also, characteristic peaks of α-Fe_2O_3 which have also been marked have appeared and it is in agreement with results of Bharathi et al [35]. The size of spherical α-Fe_2O_3 particles supported on the surface of 12-TSA.7H_2O were calculated using XRD and Warren-Averbach method (taking account of device errors) [40] whose averages were 70.82 nm. The BET surface area of α-Fe_2O_3/12-TSA.7H_2O was determined 39.84 (m^2/g).

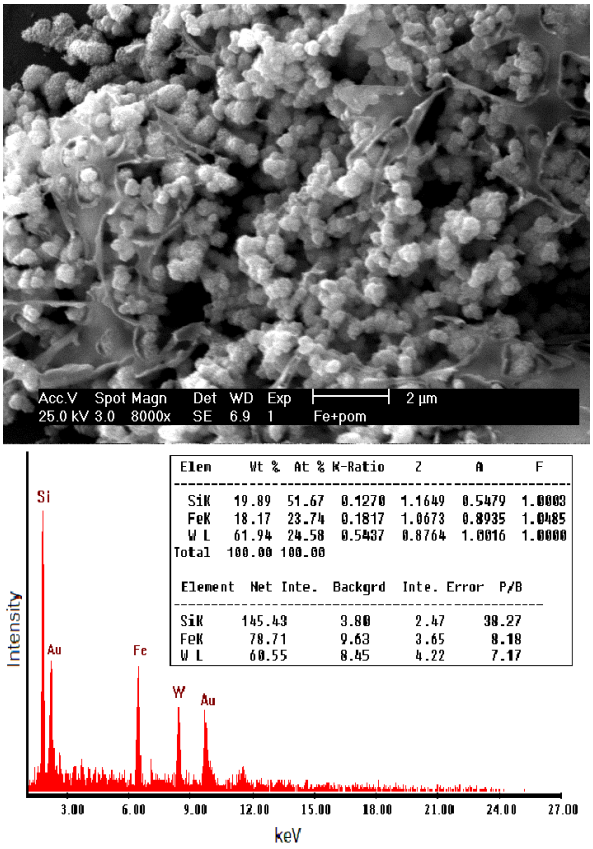

Figure 7. SEM image (top) and EDX re (bottom) of α-Fe_2O_3/12-TSA.7H_2O.

UV/Vis spectra

The absorbance of TC solutions during photocatalytic process (according to Exp. No. 15) at initial and after 10, 20, 30, 40 and 50 min irradiation time verses wavelength are depicted in Figure 8. Also, the absorbance of DC solutions (based on Exp. No. 11) at initial and after 20, 40, 60, 80, 100 and 120 min irradiation time has been shown in Figure 9.

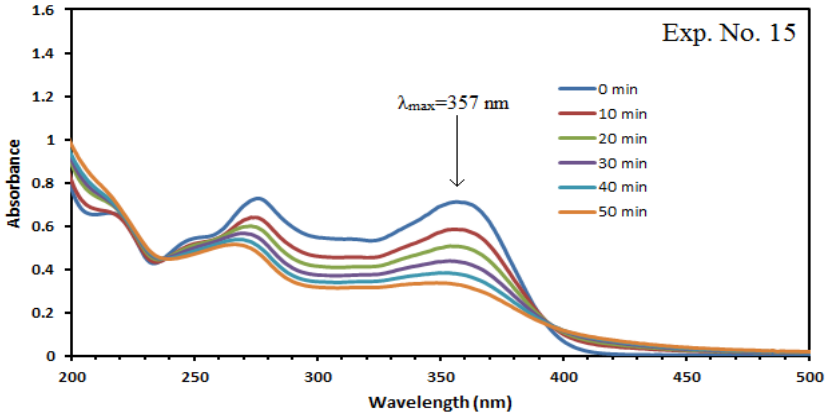

Figure 8. UV/Vis spectral absorption changes of TC solution photodegraded by α-Fe_2O_3/12-TSA.7H_2O (pH=8, Initial concentration of TC=70 ppm, catalyst concentration=50 ppm, H_2O_2 concentration=0.5 ppm).

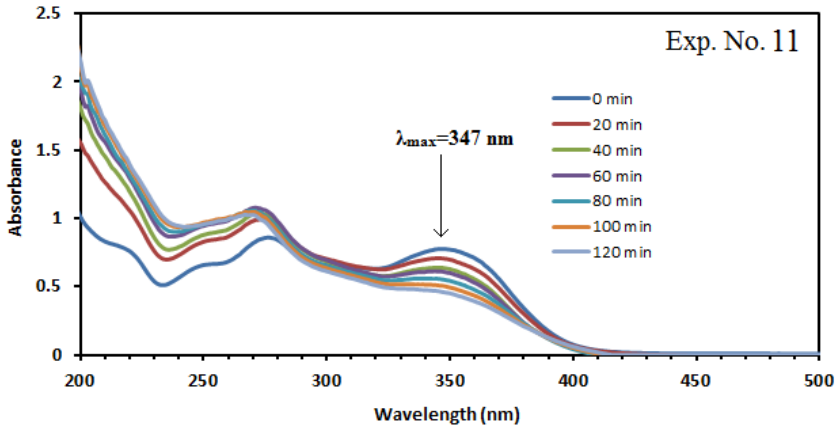

Figure 9. UV/Vis spectral absorption changes of DC solution photodegraded by α-Fe_2O_3/12-TSA.7H_2O (pH=4, Initial concentration of DC=120 ppm, catalyst concentration=100 ppm, H_2O_2 concentration=1 ppm).

Performance of photocatalysts

Having carried out all experiments based on Table 1, x% values were calculated which have been reported in Table 4. In general, comparing x% values reveal that the degree of pollutants photocatalytic degradation by pure α-Fe_2O_3 is lower than that of α-Fe_2O_3/12-TSA.7H_2O. This means that supporting α-Fe_2O_3 NPs leads to increase their photocatalytic activity. Also, the results show that in the best manner, 88.44 % TC and 87.67 % DC were degraded using α-Fe_2O_3/12-TSA.7H_2O.

Table 4. x% values

Exp. No.	x%			
	α-Fe_2O_3		α-Fe_2O_3/12-TSA.7H_2O	
	TC	DC	TC	DC
1	64.11	62.24	66.32	78.19
2	75.39	60.33	85.95	74.65
3	67.56	75.27	73.29	84.62
4	48.83	51.16	53.22	72.66
5	37.14	36.62	45.07	64.93
6	36.97	54.37	60.38	74.08
7	82.17	55.72	88.44*	83.09
8	37.95	38.4	43.64	66.15
9	65.46	60.78	74.61	72.99
10	44.37	53.32	47.92	73.67
11	32.84	36.59	38.91	65.17
12	62.00	60.83	74.28	74.66
13	29.84	44.43	37.71	69.22
14	40.69	65.77	48.72	80.09
15	39.31	52.81	45.62	73.09
16	37.02	54.45	59.79	74.44
17	66.83	81.15	77.13	87.67*
18	36.83	53.97	60.13	73.78
19	65.83	52.43	80.86	73.28

* Maximum value of x%

Photocatalytic mechanism

According to Exp. Nos. 7 and 17, the effects of UV irradiation, H_2O_2, pure α-Fe_2O_3 NPs and α-Fe_2O_3/12-TSA.$7H_2O$ on the degradation of TC and DC are presented in Figures 10 and 11, respectively. Figure 10 designate that in the presence of α-Fe_2O_3/12-TSA.$7H_2O$, H_2O_2 and UV irradiation 88.44% of TC was degraded at the reaction time of 50 min while it was 82.17% and 10.2% for pure α-Fe_2O_3 NPs and only UV, respectively. These values for DC following 120 min reaction were 87.67, 81.15 and 8.7, respectively (see Figure 11).

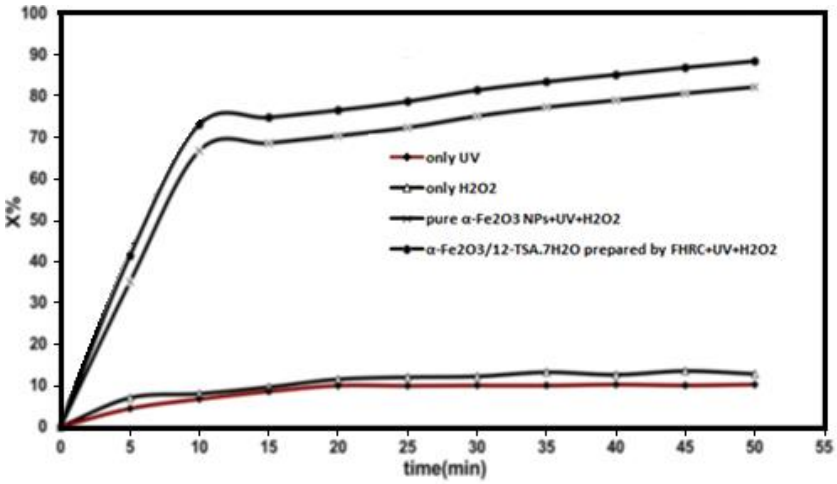

Figure 10. Effect of UV light, H_2O_2, α-Fe_2O_3 and α-Fe_2O_3/12-TSA.$7H_2O$ on TC degradation.

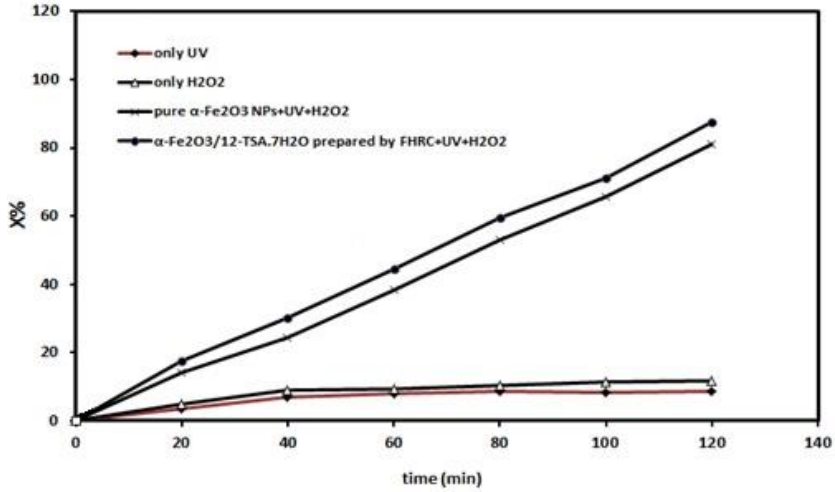

Figure 11. Effect of UV light, H_2O_2, α-Fe_2O_3 and α-Fe_2O_3/12-TSA.$7H_2O$ on DC degradation.

When α-Fe_2O_3 is illuminated by the light, electrons are promoted from the valence band (VB) to the conduction band (CB) of the semi conducting oxide to give electron-hole pairs. The VB potential (h_{VB}) is positive enough to generate hydroxyl radicals at the surface, and the CB potential (e_{CB}) is negative enough to reduce molecular oxygen. The hydroxyl radical is a powerful oxidizing agent and

attacks TC or DC molecules present at or near the surface of α-Fe_2O_3. It causes the photo-oxidation of TC or DC according to the following reactions [41, 42]:

(3) α-Fe_2O_3 + $h\nu$ → α-Fe_2O_3 (e^-_{CB} + h^+_{VB})
(4) h^+_{VB} + $H_2O_{(ads)}$ → H^+ + $^{\bullet}OH^-_{(ads)}$
(5) h^+_{VB} + $OH^-_{(ads)}$ → $^{\bullet}OH_{(ads)}$
(6) e^-_{CB} + $O_{2(ads)}$ → $^{\bullet}O^-_{2(ads)}$
(7) H_2O □ H^+ + OH^-
(8) $^{\bullet}O^-_{2(ads)}$ + H^+ → $^{\bullet}HO_2$
(9) 2 $^{\bullet}HO_2$ → H_2O_2 + O_2
(10) H_2O_2 + α-Fe_2O_3 (e^-_{CB}) → $^{\bullet}OH$ + OH^- + α-Fe_2O_3
(11) $^{\bullet}OH_{(ads)}$ + TC or DC → Degradation of TC or DC
(12) h^+_{VB} + TC or DC → $TC^{\bullet+}$ or $DC^{\bullet+}$ → Oxidation of TC or DC

The above mechanism is summarized in Figure 12. The main role of the catalyst support is creating the perfect conditions for putting the TC or DC and hydroxyl radical beside each other. Photocatalytic activity increased after stabilizing iron oxide on 12-TSA.7H_2O. To comment on this result, we propose that the hydroxyl radicals, on the surface of iron oxide, are easily transferred onto the surface of 12-TSA.7H_2O. That means the organic pollutants such as TC and DC, which have already been adsorbed on the nonphotoactive α-Fe_2O_3/12-TSA.7H_2O, have chances to be degraded due to the appearance of hydroxyl radicals, resulting in the enhancement of the photodegradation performance of α-Fe_2O_3/12-TSA.7H_2O (as shown in Figure 12b).

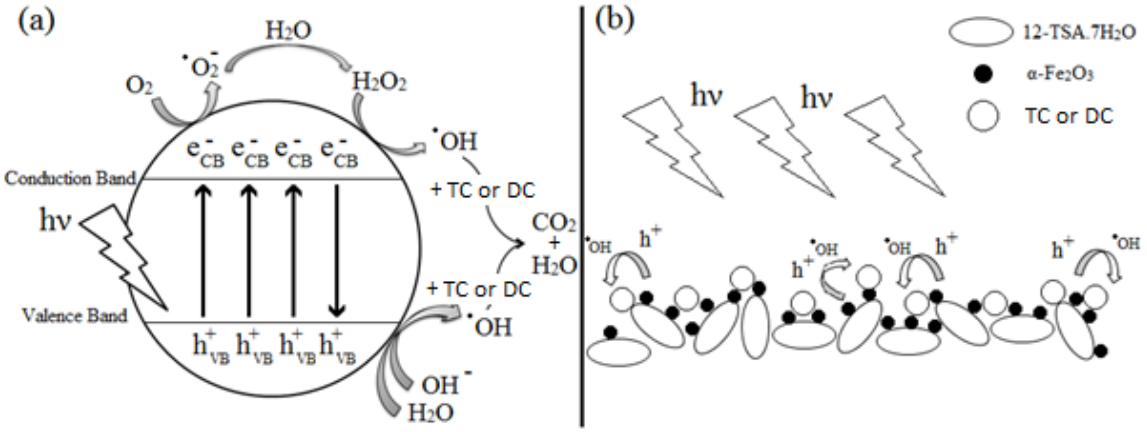

Figure 12. General mechanism of the photocatalysis (a) and photocatalytic activity of α-Fe_2O_3/12-TSA.7H_2O (b).

Kinetics of photocatalytic degradation of pollutants

Figures 13 and 14 displays the plot of $\ln(C_0/C)$ versus reaction time for TC and DC, respectively. The linearity of the plots suggests that the photodegradation reactions approximately follows the pseudo-first order kinetic with a rate coefficient k=0.017 min^{-1} and 0.0074 min^{-1} for TC and DC, respectively. So that, kinetic equations are as below:

(13) R_{TC}=0.017 [TC]

(14) R_{DC}=0.0074 [DC]

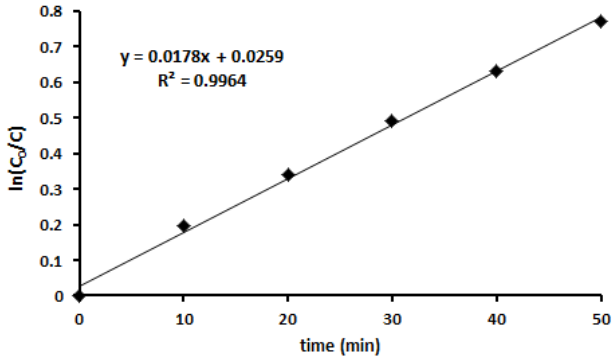

Figure 13. Plot of reciprocal of pseudo-first order rate constant against pH=8, Initial concentration of TC=30 ppm, catalyst concentration=150 ppm, H_2O_2 concentration=0.1 ppm.

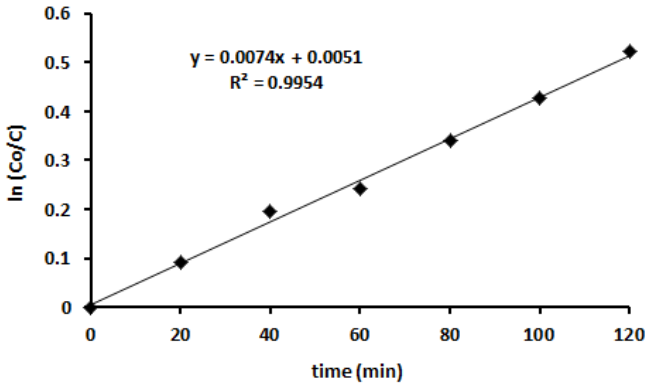

Figure14. Plot of reciprocal of pseudo-first order rate constant against pH=4, Initial concentration of DC=80 ppm, catalyst concentration=150 ppm, H_2O_2 concentration=2 ppm.

The statistical analysis

Analysis of variance (ANOVA) is a set consists of a number of statistical methods used to analyze the differences among group means and their associated procedures. ANOVA was used for graphical analyses of the data to obtain the interaction between the process variables and the responses. The effect on the response was increased by increasing the value of F parameter and decreasing P parameter. The quality of the fit polynomial model was expressed by the coefficient of determination (R^2), and its statistical significance was checked by the Fisher's F-test in the same program. Model terms were evaluated by the P-value. The estimated effects and coefficients of TC and DC degradation processes have been listed in Tables 5 and 6, respectively. In these tables, standard deviation (S), correlation coefficient, pred R-squared and adjusted R-squared values were also reported. The R^2 value is always between 0 and 1. The closer the R^2 value to 1, the stronger the model is and the better the model predicts the response (x%). R^2 values were reported to be 0.9994 and 0.9954 for TC and DC processes, respectively. Due to Table 5 and the significant variables effects on the

response, affect magnitudes of the initial concentration of TC, pH, H_2O_2 concentration and catalyst concentration equal to 32.51, 2.19, 3.32 and 7.22, respectively. Thus, the significant reaction parameters were (the most to the least significant): initial concentration of TC > catalyst concentration > H_2O_2 concentration > pH. Of course, it is necessary to note that despite other three variables, the variable of the initial concentration of TC has a negative effect on the response (–32.51). This means that increasing the initial concentration of TC leads to decrease x% and conversely. In this way, the effects about the variables interaction were reported in Table 5. As can be seen from these results, it is the only interaction of variables, namely pH and the catalyst concentration which have positive effects (1.57). The interaction of the initial concentration of TC with pH, pH with catalyst concentration and H_2O_2 concentration with catalyst concentration have both negative and roughly the same effects on the x% value (–4.23, –1.33 and –3.39, respectively). In Table 5, the coefficients of each term have been reported which are the same term coefficients in response function which they will be given in the following. It is vital to note that P values have been assessed considering Alpha=α=0.05. Table 6 (that is related to the process of DC degradation) shows that initial concentration of DC variable has the highest effect on the response (–6.974). The variables of initial concentration of DC and pH have negative effects and variables of H_2O_2 concentration and catalyst concentration have positive effects on the response. Also, it is seen that the effect of interaction among pH and catalyst concentration is negative (–6.221), while it has the highest effect on the response among other 2-way interactions. In Table 7, complementary results have been listed which have been used for drawing residual plots. Residual values were calculated from subtracting experimental x% values and fitted values.

Table 5. Estimated effects and coefficients for TC degradation process

Term	Effect	Coef	SE Coef	T (Coef/SE Coef)	F value	P value	Result
Constant	-	61.36	0.1711	358.59	-	<0.0001	Significant
Initial Con. of TC	–32.51	–16.25	0.1711	–95.00	9025.02	<0.0001	Significant
pH	2.19	1.09	0.1711	6.40	40.91	0.001	Significant
H_2O_2 Con.	3.32	1.66	0.1711	9.70	94.06	<0.0001	Significant
Catalyst Con.	7.22	3.61	0.1711	21.11	445.62	<0.0001	Significant
Initial Con. of TC×pH	–4.23	–2.12	0.1711	–12.36	152.87	<0.0001	Significant
pH×H_2O_2 Con.	–1.33	–0.67	0.1711	–3.90	15.19	0.008	
pH×Catalyst Con.	1.57	0.78	0.1711	4.58	20.95	0.004	
H_2O_2 Con.×Catalyst Con.	–3.39	–1.70	0.1711	–9.92	98.36	<0.0001	Significant
Center point	-	–2.13	–1.26	–2.92	-	0.027	

S=0.6844, R^2=99.94%, Pred R^2=99.11%, Adj R^2=99.82%

Table 6. Estimated effects and coefficients for DC degradation process

Term	Effect	Coef	SE Coef	T (Coef/SE Coef)	F value	P value	Result
Constant	-	73.608	0.128	575.55	-	<0.0001	Significant
Initial Con. of DC	–6.974	–3.487	0.139	–25.02	625.97	<0.0001	Significant
pH	–3.739	–1.869	0.139	–13.41	179.92	<0.0001	Significant
H_2O_2 Con.	2.596	1.298	0.139	9.31	86.76	<0.0001	Significant
Catalyst Con.	4.341	2.171	0.139	15.57	242.58	<0.0001	Significant
pH×Initial Con. of DC	2.949	1.474	0.139	10.58	111.92	<0.0001	Significant
pH×Catalyst Con.	–6.221	–3.111	0.139	–22.32	498.17	<0.0001	Significant
pH×H_2O_2 Con.	0.959	0.479	0.139	3.44	11.83	0.007	
Initial Con. of DC×H_2O_2Con.	2.659	1.329	0.139	9.54	90.99	<0.0001	Significant
Catalyst Con. ×H_2O_2Con.	2.884	1.442	0.139	10.35	107.04	<0.0001	Significant
Center point	-	–1.67	1.116	–0.722	-	0.034	

S=0.557465, R^2=99.54%, Pred R^2=97.11%, Adj R^2=99.08%

Table 7. Residual values

Exp. No.	For TC process			For DC process		
	x%	Fit	Residual (x%–Fit)	x%	Fit	Residual (x%–Fit)
1	66.32	66.7703	-0.4503	78.19	76.79082	1.399178
2	85.95	85.3212	0.6288	74.65	81.47457	-6.82457
3	73.29	73.4112	-0.1212	84.62	83.37207	1.247928
4	53.22	53.0988	0.1212	72.66	71.80082	0.859178
5	45.07	44.4022	0.6678	64.93	71.01082	-6.08082
6	60.38	60.1000	0.2800	74.08	74.54895	-0.46895
7	88.44	89.1078	-0.6678	83.09	78.77957	4.310428
8	43.64	44.1281	-0.4881	66.15	68.91957	-2.76957
9	74.61	74.5137	0.0963	72.99	72.19832	0.791678
10	47.92	48.5488	-0.6288	73.67	73.70582	-0.03582
11	38.91	38.4597	0.4503	65.17	68.51707	-3.34707
12	74.28	74.3372	-0.0572	74.66	72.60082	2.059178
13	37.71	37.8063	-0.0963	69.22	67.72707	1.492928
14	48.72	48.8022	-0.0822	80.09	74.49582	5.594178
15	45.62	45.5628	0.0572	73.09	68.12957	4.960428
16	59.79	60.1000	-0.3100	74.44	74.54895	-0.10895
17	77.13	77.0478	0.0822	87.67	86.06707	1.602928
18	60.13	60.1000	0.0300	73.78	74.54895	-0.76895
19	80.86	80.3718	0.4882	73.28	77.19332	-3.91332

Figure 15 shows the graphical results of TC degradation process. In order to compare the variables effect (from the viewpoint of magnitude) on the response, the Figure 15a could be investigated which is one Pareto chart of the standardized effects. In this Figure, those variables whose effects on response is negative (–) or positive (+) have been marked. The results revealed that the effect of the initial concentration of TC on the x% is greater than other variables effect (at least four times) but the effect of this variable is negative i.e. increasing or

decreasing the initial concentration of TC leads to decrease and increase x%, respectively. In order to better investigate the residual values, residual plot versus Exp. No. has been illustrated in Figure 15b. As it is seen, nine points (residuals) are located under zero line (negative) and ten points above zero line (positive). Due to this and comparing distance of points from zero line, it could be said that residual distribution is normal. An extremely useful procedure is to construct a normal probability plot of the residuals. If the underlying error distribution is normal, this plot will resemble a straight line. Figure 15c shows normal probability plot. In this plot, it is fully clear that residuals distribution is normal because points (especially central points) are close to straight line. If the model is correct and if the assumptions are satisfied, the residuals should be structure less; in particular, they should be unrelated to any other variable including the predicted response. A simple check is to plot the residuals versus the fitted values. Figure 15d displays plot of residuals versus fitted values. Graphical results of DC degradation process have been illustrated in Figure 16. Pareto chart in Figure 16a shows that greatest and smallest effect on the response were respectively related to initial concentration of DC and interaction among pH and H_2O_2 concentration variables. The uniform distribution of points above and below the zero line in Figure 16b shows that residuals in experiments of DC degradation process are normally distributed. Also, normal probability plot of the process has been illustrated in Figure 16c which proximity of points to the line and centralization of points indicate the normality of residuals. Mathematical models representing TC and DC photocatalytic degradation in the range studied can be expressed by the following equations, respectively:

Response = x% (TC) = 61.36 – 16.25 A + 1.09 B + 1.66 C + 3.61 D – 4.23 AB – 1.33 BC + 1.57 BD – 3.39 CD + 3.97 ABC – 4.00 ABD + 1.59 BCD ± . . .

Response = x% (DC) = 73.608 – 3.487 A – 1.869 B + 1.298 C + 2.171 D + 1.474 BA – 3.111 BD + 0.479 BC + 1.329 AC + 1.442 DC ± . . .

Where A, B, C and D are the initial concentration of pollutant, pH, H_2O_2 concentration and catalyst concentration, respectively.

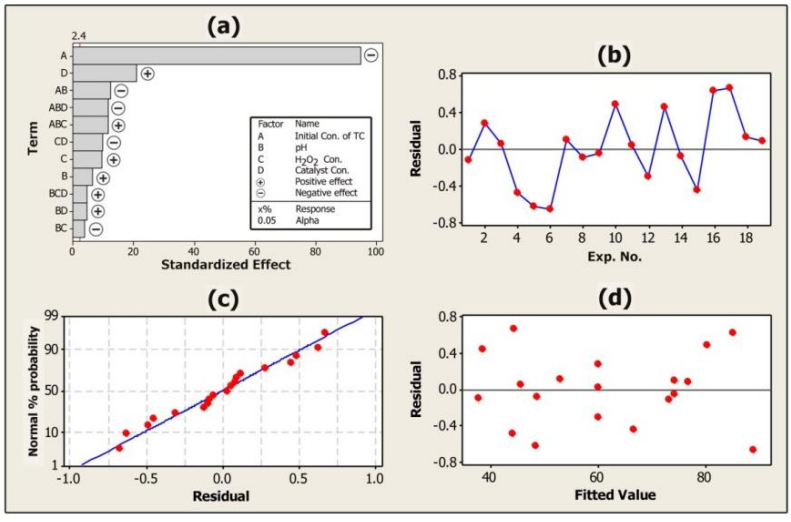

Figure 15. (a) Pareto chart of the standardized effects, (b) plot of residuals versus Exp. No., (c) Normal probability plot and (d) plot of residuals versus fitted values related to TC degradation process.

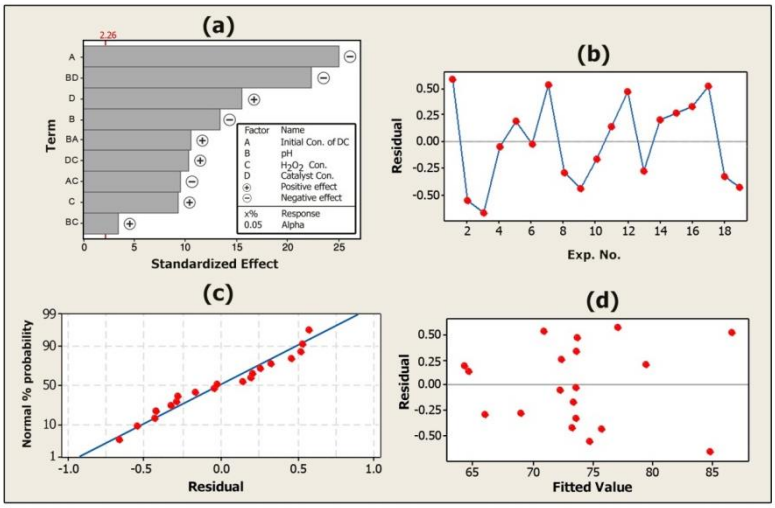

Figure 16. (a) Pareto chart of the standardized effects, (b) plot of residuals versus Exp. No., (c) Normal probability plot and (d) plot of residuals versus fitted values related to DC degradation process.

In Figure 17, the plots of main effects related to TC degradation process have been shown. These plots indicate that of four main effects, only the variable of the initial concentration of TC has a negative effect on response; effects of other variables on response were positive. In effect, increasing the initial concentration of TC and decreasing pH, H_2O_2 concentration and catalyst concentration will be caused to decrease and increase x%, respectively (if the interaction effect of variable is ignored). The slope of line in main effect plots is one indicator of magnitude related to the variable effect on the response. Therefore, the order of affecting variables from magnitude viewpoint is as initial concentration of TC > catalyst concentration > H_2O_2 concentration > pH which confirm the results of Figure 15a. The plots of main effects (related to the process of DC degradation) have been illustrated in Figure 18. These plots show that as the level of initial concentration of DC and pH variables increase, then the response decreases and as the level of H_2O_2 concentration and catalyst concentration variables increase, then the response increases. Also, because the plots of initial concentration of DC and H_2O_2 concentration variables have highest and lowest slope respectively, then they have greatest and smallest effects on the response, respectively.

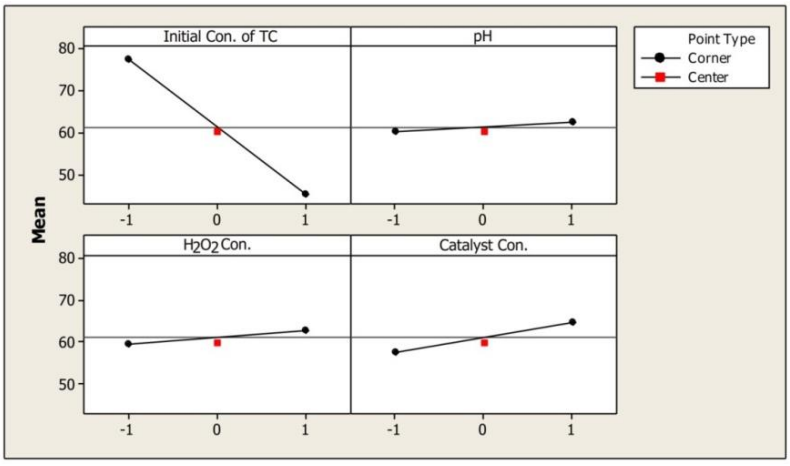

Figure 17. Main effects plot for TC degradation process.

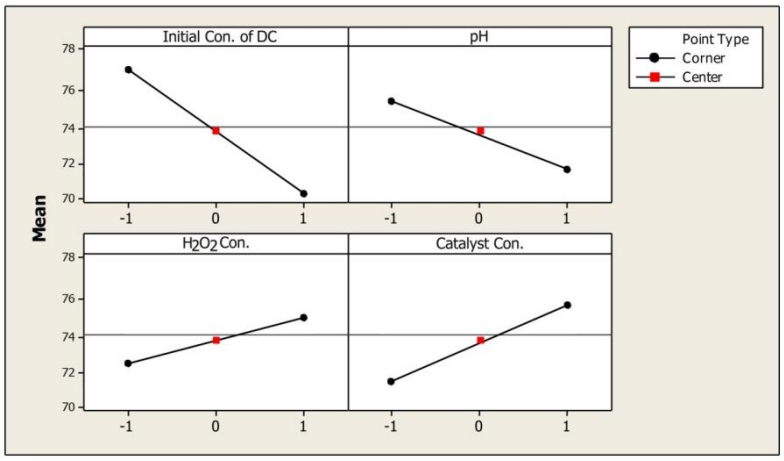

Figure 18. Main effects plot for DC degradation process.

In Figure 19, interaction plots for TC degradation process have been presented. Generally, in such plots the more parallel the lines, the lower the interaction effect would be and the more intersecting the lines, the higher the interaction effect would be. As it is observed, there is a significant interaction effect among pH and H_2O_2 concentration, pH and catalyst concentration, H_2O_2 concentration and catalyst concentration variables. Generally, considering the interaction effects is very important because it may place the unpredictable effects on the response. For example, based on the results of Figure 15a even though H_2O_2 concentration had simply a positive effect on x%, the maximum x% was achieved in those conditions where H_2O_2 concentration was at its minimum level (see Exp. No 7 in Table 4). For the same reason, the interaction effect of variables should not be ignored in studying variables for reaching optimal conditions. In Figure 20, Interaction plots of DC degradation process have been shown. It is seen that there is significant interaction between pH and catalyst concentration variables. This interaction among pH and initial concentration of DC variables and also between catalyst concentration and H_2O_2 concentration are rather found.

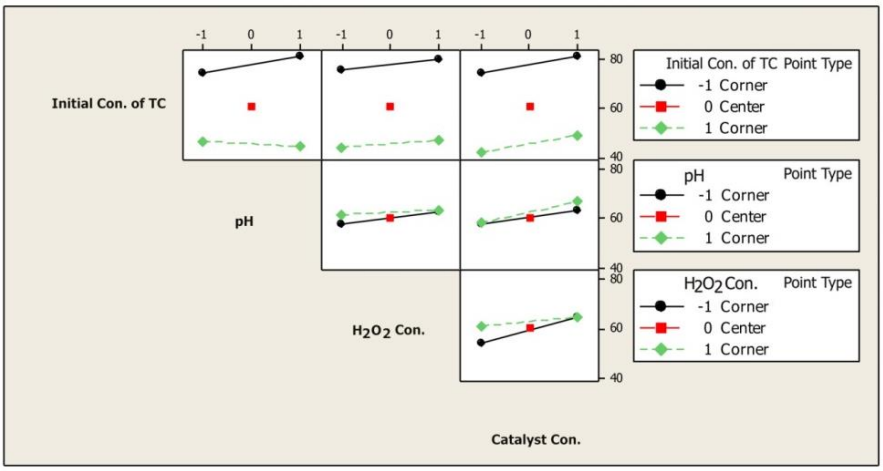

Figure 19. Interaction plot for TC degradation process.

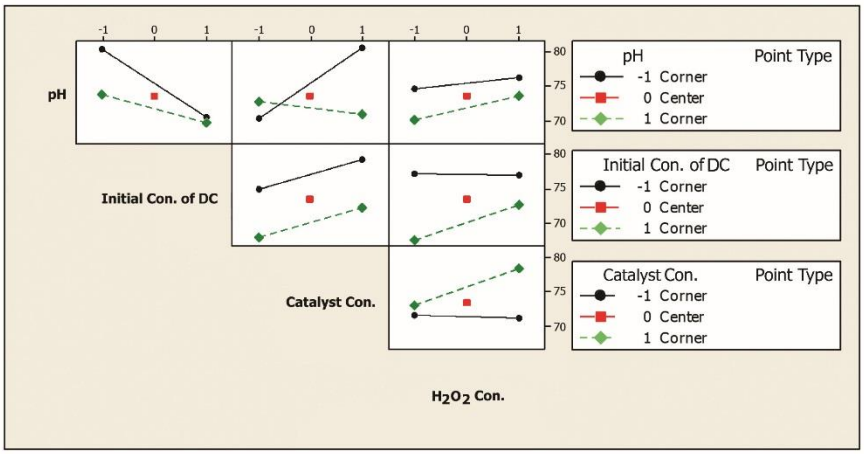

Figure 20. Interaction plot for DC degradation process.

Conclusions

The results revealed that:

1. Spherical α-Fe_2O_3 NPs had been successfully synthesized and supported on the surface of 12-TSA.7H_2O through FHRC method with no decrease of NPs photocatalytic efficiency and chemical change of 12-TSA.7H_2O which are indicative of being effective this supporting method.
2. While supporting α-Fe_2O_3 NPs on the surface of 12-TSA.7H_2O help to recover them from the medium and reusing them, it causes to enhance their photocatalytic activities.
3. Photocatalytic effect of α-Fe_2O_3/12-TSA.7H_2O on the TC and DC degradation is greater than pure α-Fe_2O_3 NPs.
4. The statistical analysis results indicated that the model used in this paper is significantly reliable and valid.
5. In the processes of the TC and DC photocatalytic degradation using α-Fe_2O_3/12-TSA.7H_2O, four parameters of pH, the initial concentration of pollutant, catalyst concentration and H_2O_2 concentration are effective on x%.
6. The interaction effects of variables are very important and should be considered for optimizing the conditions because it significantly affects the x%.
7. The optimum conditions for the TC degradation process by α-Fe_2O_3/12-TSA.7H_2O is as pH=8, initial concentration of TC=150 ppm, catalyst concentration =150 ppm and H_2O_2 concentration=0.1 ppm so that they cause to reach maximum degradation (88.44%).
8. The optimum conditions for the DC degradation process is as pH=4, initial concentration of DC=80 ppm, catalyst concentration =150 ppm and H_2O_2 concentration=2 ppm so that they cause to reach maximum degradation (87.67%).
9. The kinetics of TC and DC photocatalytic degradation reactions are of the pseudo-first order with k=0.0178 and 0.0074 min^{-1}, respectively.

Acknowledgments: This work was financially supported by Islamic Azad University of Arak, Iran.

References

[1] Novo. A, Andre. S, Viana. P, Nunes. O. C, Manaia. C. M, Water. Res, 2013, 47, 1875.
[2] Kummerer. K, Chemosphere, 2013, 75, 417.

[3] Brown. K. D, Kulis. J, Thomson. B, Chapman. T. H, Mawhinney. D. B, Sci. Total Environ. 2066, 366, 772.
[4] Pailler. J. Y, Krein. A, Pfister. L, Hoffmann. L, Guignard. C, Sci. Total Environ. 2009, 407, 4736.
[5] Hou. J, Wang. C, Mao. D, Luo. Y, Environ. Sci. Pollut. Res. Int. 2016, 23, 1722.
[6] Pourmoslemi. S, Mohammadi. A, Kobarfard. F, Amini. A, Water Sci. Technol. 2016, 74, 1658.
[7] Neatu. S, Macia-Agullo. J. A, Concepcion. P, Garcia. H. J, Am. Chem. Soc. 2014, 136, 15969.
[8] Chen. M, Liu. J, Chao. D, Wang. J, Yin. J, Lin. J, Fan. H. J, Shen. Z. X, Nano Energy, 2014, 9, 364.
[9] Rancourt. D. G, Julian. S. R, Daniels. J. M. J, Magn. Mater. 1985, 49, 305.
[10] Hill. C. L, Chem. Rev. 1998, 98, 1.
[11] Pope. M. T, Heteropoly and Isopoly Oxometalates, SpringerVerlag, Berlin, 1983.
[12] Kozhevnikov. I. V, Chem. Rev. 1998, 98, 171.
[13] Es'haghi. Z, Hooshmand. S. J, Sep. Sci. 2015, 38, 1610.
[14] Wang. L. Zhou. B, Liu. J, Prog. Chem. 2013, 25, 1131.
[15] Judd. D. A, Netlles. H. J, Nevis. N, Snyder. J. P, Liotta. D. C, Tang. J, Ermolieff. J. J, Schinazi. F. R, Hill. C. L. J, Am. Chem. Soc. 2001, 123, 886.
[16] Wang. X, Liu. J, Li. J, Liu. J, Inorg. Chem. Commun. 2001, 4, 372.
[17] Lin. Z, Zhongqun. L, Wenjun. C, Shaojin. C, Radioanal. J. Nucl. Chem. 1996, 205, 49.
[18] Heylen. S, Smeekens. S, Kirschhock. C. E. A, Parac-Vogt. T. N, Martens. J. A, Energy Environ. Sci. 2010, 3, 910.
[19] Lihua. B, Qizhuang. H, Qiong. J, Enbo. W. J, Mol. Struct. 2001, 597, 83.
[20] Xia. Y, Xiong. Y, Lim. B, Skrabalak Angew. S. E, Chem. Int. Ed. 2009, 48, 60.
[21] Zhang. S, Fan. Q, Gao. H, Huang. Y, Liu. X, Li. J, Xu. X, Wang. X. J, Mater. Chem. A. 2016, 4, 1414.
[22] Zhang. S. Li. J, Wang. X, Huang. Y, Zeng. M, Xu. J. J, Mater. Chem. A. 2015, 3, 10119.
[23] Jun. Y. W, Choi. J. S, Cheon. J.J, Chem. Commun. 2007, 12, 1203.
[24] Chen. J, Xu. L, Li. W, Gou. X, Adv. Mater. 2005, 17, 582.
[25] Raming. T. P, Winnubst. A. J. A, Van Kats. C. M, Philipse. A. P. J, Colloid Interface. Sci. 2002, 249, 346.
[26] Walter. D, Thermochim. Acta 2006, 445, 195.
[27] Shekhah. O, Ranke. W, Schule. A, Kolios. G, Schlogl. R, Angew. Chem. Int. Ed. 2003, 42, 5760.
[28] Mishra. M, Chun. D. M, Appl. Catal. A 2015, 498, 126.
[29] Farahmandjou. M, Soflaee. F, Phys Chem. Res. 2015, 3, 191.
[30] Liang. H, Liu. K, Ni. Y, Mater. Lett. 2015, 159, 218.
[31] Diab. M, Mokari. T, Inorg. Chem. 2014, 53, 2304.
[32] Jiang. T, Poyraz. A. S, Iyer. A, Zhang. Y, Luo. Z, Zhong. W, Miao. R, El-Sawy. A. M, Guild. C. J, Sun. Y, Kriz. D. A, Suib. S. L. J, Phys. Chem. 2015, 119, 10454.
[33] Askarinejad. A, Bagherzadeh. M, Morsali. A. J, Exp. Nanosci. 2011, 6, 217.
[34] Tadic. M, Panjan. M, Damnjanovic. V, Milosevic. I, Appl. Surf. Sci. 2014, 320, 183.
[35] Bharathi. S, Nataraj. D, Mangalaraj. D, Masuda. Y, Senthil. K, Yong. K. J, Phys. D, Appl. Phys. 2010, 43, 1.
[36] Nabizadeh. R, Jahangiri Rad. R, Res. J. Nanosci. Nanotechnol, 2016, 6, 1.
[37] North. E. O, Bailar. J. C, Jonelis. F. G, Inorg. Synth. 2007, 1, 129.
[38] Bamoharram. F. F, Molecules 2009, 14, 3214.

[39] Kozhevnikov. I. V, Sinnema. A, Jansen. R. J. J, Bekkum. H. V, Catal. Lett. 1994, 27, 187.
[40] Enzo. S, Polizzi. S, Benedetti. A, Zeitschrift für Kristallographie 1985, 170, 275.
[41] Yao. K, Basnet. P, Sessions. H, Larsen. G. K, Hunyadi Murph. S. E, Zhao. Y, Catal. Today 2016, 270, 51.
[42] Guo. S, Zhang. G, RSC Adv. 2016, 6, 2537.

Communications In Catalysis
Vol. 1, No. 2, 2024, pp.57-64
DOI: 10.22049/CIC.2018.26358.1023
Azarbaijan Shahid Madani University

Study of volumetric and electromagnetic properties of binary and ternary mixtures of {2-Propanol (1) + 1, 3-Diaminopropane (2) + 2, 5- Dimethoxytetrahydrofuran (3)} at (298.15- 328.15) K at 81.5 kPa-Prediction with geometrical models

Farnoosh. Panahi, Mahdi. Jafarnejad*, Khatereh. Khanlarzadeh, Hossein. Iloukhani

Department of Physical chemistry, Faculty of Chemistry, Bu-Ali Sina University, P.O. Box 65178-38695, Hamedan, Iran.

*Corresponding Author: Tel: +988138381601, Fax: +988138380663.

E-mail address: me.jafarnejad@gmail.com

Received: 2024-12-15, Revised: 2025-01-18, Accepted: 2025-01-30

Abstract

The densities, ρ and refractive index,n_D of mixtures consisting of 2-Propanol, 1, 3-Diaminopropane, and 2, 5-Dimethoxytetrahydrofuran have been measured at different temperatures. V_m^E, $\overline{V^E}_{m,i}$, ,Δn_D, $\alpha^E$and $(\partial H_m^E/\partial P)_{T,x}$ for binary and $V_m^E$and Δn_D for ternary mixtures were derived. V_m^E and Δn_D for binary mixtures were correlated with the Redlich–Kister equation and for ternary mixtures were correlated with several equations. Prediction geometrical solution models were used to predict $\overline{V^E}_{m,i}$, $\Delta n_D$of ternary mixtures and standard deviation for their fitting was reported. Positive deviation from ideal state were recorded for $\overline{V^E}_{m,i}$ in mixture of 1, 3-Diaminopropane + 2, 5-Dimethoxytetrahydrofuran and 2-Propanol + 2, 5-Dimethoxytetra-hydrofuran mixtures. However, in mixture of 2-Propanol and 1, 3-Diaminopropane negative deviation in the high composition of 1, 3-Diaminopropane varies to positive in the dominated mole fraction of alcohol which was analyzed to interpret the molecular interactions.

Keywords: Ternary mixtures, Volumetric properties, Refractive index, Molecular interactions, Prediction models

Introduction

The main branch in the study of solutions is the investigating of the thermodynamic properties of the mixtures. Thermodynamics and thermodynamic properties have been of interest for researchers for many years in the various fields of science, technology and industry in particular, and have been widely studied. The properties of the solutions that are studied in this work are the most complex thermodynamic quantities due to various factors such as structural effects, interactions between similar and non-similar components, and are very useful in explaining and justifying interactions and renovating due to the mixing process. Due to the fact that most of the biological and industrial processes are in the liquid phase, the solubility phenomenon is very important and the solvent effect is very important on soluble properties. Among the issues that researchers and chemists investigate in this regard, is the importance of solubility of materials and changes in the thermo physical properties of compounds as a result of solubility in the processes of separation and purification. Interpretation and justification of the nature of molecular interactions are widely used in these processes, and the knowledge of these interactions is possible by measuring and computing the Physico-chemical characteristics and thermodynamic properties of these systems. These interactions are influenced by short-range repulsive forces and long-range molecular attraction with the effects of polarity and etc., that the correct understanding of the nature and intensity of these forces helps us to understand and interpret the interactions.

Thermodynamic properties of mixtures of amines, methoxy and hydroxyl groups are seemed to be interesting and would give great outcomes of molecular interactions in solutions. Meanwhile the studies of volumetric and electromagnetic properties of liquid mixtures provide valuable information on the structure and molecular interactions in solutions. In this sense, structural changes as a result of the molecular interaction can be provided by investigating the deviation of the refractive index deviations and volumetric properties from the ideal state due to compositions and temperatures. The deviations in the properties of solutions from the ideal state result from the breaking of the bonds of primary pure components and the formation of new bonds between non-similar molecules.

In fact, these deviations are affected by three factors: a physical, chemical, and molecular structure that includes breaking the dipole-dipole, ionic, and hydrogen bonds and causes positive deviation or forming solvent-soluble bonds, which can be even hydrogen and dipolar type with proper orientation in some of the molecules that lead to negative deviations. In addition to these factors, the steric effect result of some large groups, as well as diversity in size and shape of components in mixtures are effected deviations substantially [1, 2].

The aim of our research group is developing the thermodynamic data for analysis and identification of molecular interactions in non-electrolyte solutions at different temperatures [3-5]. In this regard, present paper reports the density, ρ, and excess molar volume, V_m^E, refractive index deviations Δn_D of 2-

Propanol(1) + 1, 3-Diaminopropane (2) + 2, 5-Dimethoxytetrahydrofuran (3) and its corresponding binary systems at different temperatures (298.15, 308.15, 318.15, and 308.15) K and at ambient pressure. Also, Partial excess molar volumes $\overline{V^E}_{m,i}$, excess thermal expansion coefficient α^E and isothermal coefficient of pressure excess molar enthalpy $(\partial H_m^E/\partial P)_{T,x}$ for binary mixtures were reported. Data for the binary systems was fitted to Redlich–Kister equation [6, 7] and for ternary mixtures were correlated with Cibulka [8], Singe [9], Jasinski and Malanowski[10], Calvo [10], Nagata [11] equations and parameters have also been calculated.

2. Experimental

2.1. *Materials*

The 2-Propanol (CAS No. 67-63-0), 1, 3-Diaminopropane (CAS No. 109-76-2), and 2, 5-Dimethoxytetrahydrofuran (CAS No. 696-59-3) were purchased from Merck, and used without any further purification. Information about the liquids employed in this work are given in Table 1. The experimental densities and refractive indices of pure materials with corresponding literature value are presented in Table 2. The pure components were stored in the dark glasses at constant humidity and temperature.

2.2. *Apparatus and procedure*

Mixtures were prepared based on sample weight, using electronic balance (Sartorious AG. GK 1203, Germany) with precision of ±0.0001 g. Density of pure components and mixtures were measured using digital vibrating-tube densimeter (Anton Paar DMA 4500), with an accuracy of ± 0.01 K in temperature. The measurement of refractive indices of pure components and mixtures were obtained by digital automatic refractometer (Anton Paar Abbemat 500) with the accuracy of ± 0.01 K in temperature. The details regarding density and refractive index measurement using Anton Paar DMA4500 and Anton Paar Abbemat 500 are described in our previous literature [3]. The estimated uncertainty for density and refractive index measurement, and mole fraction, are ± 1 × 10^{-5} g · cm^{-3}, ±5×10^{-5}, and ±4×10^{-4}.

Each system was immediately used after it was well-mixed by shaking. After measuring density and refractive index of mixtures over the temperature range T = (298.15 to 328.15) K with intervals of 10 K in ambient pressure, excess molar volume for all mixtures was calculated using density data by following equation:

$$(1)\quad V_m^E = \left(\frac{\sum_{i=0}^{n} x_i M_i}{\rho}\right) - \left(\sum_{i=0}^{n} \frac{x_i M_i}{\rho_i}\right)$$

where ρ, is the density of system, ρ_i and M_i are the density and molar mass of the pure component and x_i is the mole fraction and n is the number of components in mixture. The refractive index deviations Δn_D, for mixtures can be calculated as:

$$(2)\qquad \Delta n_D = n_D - \sum_{i=1}^{n} x_i n_{Di}$$

Where n_D is the refractive index of the mixture and n_{Di} is the refractive index of

pure components,i and n is the number of components in mixture.

3. Results and discussion

3.1 Binary mixtures

The excess molar volume for binary mixtures was calculated from density results according to equation (1) with uncertainty of $\pm 8\times10^{-3}$ $cm^3.mol^{-1}$. Excess molar volumes for binary systems are appeared in Table 3 and are graphically represented in Figure1. The experimental data of the binary systems were correlated with the following type of Redlich–Kister polynomial:

$$(3) Y_m = x(1-x)\sum_{i=0}^{k}\sum_{j=0}^{2} B_{ij}T^j\,(1-2x)^i$$

where $Y_m = (\ V_m^E or\ \Delta n_D)$; $B_{ij}$is adjustable temperature dependent parameters obtained by fitting algorithm.

The parameters B_{ij} for all the binary systems are listed in Table 4, along with standard deviation,σ, were obtained by this equation:

$$(4)\ \sigma(Y_m) = \left[\sum_{i=1}^{n}\left(Y_{m,exp.i} - Y_{m,calc.,i}\right)^2/(n-p)\right]^{1/2}$$

where *n* is the number of experimental data and *p* is the degree of the polynomials.

As can be seen in Figures1, V_m^E values for binary systems of 1, 3-Diaminopropane (1) + 2, 5-Dimethoxytetrahydrofuran (2), and 2-Propanol (1) + 2, 5-Dimethoxytetrahydrofuran (2) are positive over the whole composition range which indicates the expansion of mixing. As quantified by the Hammett equation, methoxy is an electron-donating group [12]. On the other hand, like ammonia, amines are bases [13].In fact, deviations are influenced by three physical, chemical and structural factors that include breaking or weakening bipolar-bipolar, ionic bonds, hydrogen bands, and London dispersion force, which divert the solution to positive deviations. In addition, the steric effect also has a noticeable effect on this positive deviation. These effects lead to expansion in volume of mixtures and therefore positive deviations are obtained as can be seen in Figure1 (b) – 1(c), which clearly indicate that there is a kind of repulsive interactions in these binary mixtures. But for binary system of 2-Propanol (1) + 1, 3-Diaminopropane (2) , deviation of V_m^E values in the high concentrations of 1, 3-Diaminopropane are negative which indicates attractive interactions and increasing the concentration of 2-Propanol leads to found repulsion forces which appears in Figure 1(a). In addition, interactions those cause formation of the structures result negative amounts of excess molar volume and interactions that cause structural destruction, leading to the positive amount of excess molar volume; the contribution of accumulation in the molar volume is negative.

Nevertheless, the positive deviation of V_m^E from the ideal state for the examined systems in this project shows that short-range repulsive forces are in the ruling system, which expresses the fact that due to mixing, soluble-solvent molecule interactions would weakened and

relatively strong interactions between similar molecules are formed.

Correlations are complicated owing to the effects of solvation which are opposite the trends for inductive effects. According to the calculated refractive index deviation values, the optical behavior of these systems is similar to volumetric behavior as the values specified in Table 3 and graphically presented in Figure 2. Studding effect of temperature released that as temperature of 2-Propanol + 2, 5-Dimethoxytetrahydrofuran mixture rises, V_m^Edeviations are increase but it is contrary in 1, 3-Diaminopropane + 2, 5-Dimethoxytetrahydrofuran mixture. With increasing temperature, V_m^E deviations dedicate a negative value and with further increase in temperature, a value of $V_m^E$is much less.

The partial molar volume, $\bar{V}_i$, for binary systems were calculated over the whole concentration rang by using equation (5) and the excess partial molar volume values calculated by equation (6) are reported in Table 3.

$$(5)\bar{V}_i = V_m^E + V_i^o + (1 - x_i)\left(\frac{\partial V_m^E}{\partial x_i}\right)_{p,T}$$

$$(6) \qquad \bar{V}_i = \bar{V}_i^E + V_i^*,$$

The thermal expansion coefficient α, for pure components was calculated by analytical differentiation of density fitting equation:

$$(7) \qquad \alpha = -\rho^{-1}\left(\frac{\partial \rho}{\partial T}\right)_p$$

The excess thermal expansion coefficient α^E, was obtained by the following expression:

$$(8) \qquad \alpha^E = \alpha - \sum_{i=1}^{2} x_i \alpha_i,$$

The isothermal coefficient of pressure excess molar enthalpy $(\partial H_m^E/\partial P)_{T,x}$can be derived accurately from volumetric measurements by application of the following equation:

$$(9) \qquad \left(\frac{\partial H_m^E}{\partial P}\right)_{T,x} = V_m^E - T\left(\frac{\partial V_m^E}{\partial T}\right)_{P,x}$$

The computed values of α^E *and* $(\partial H_m^E/\partial P)_{T,x}$ for binary mixtures are listed in Tables 3and at T = 298.15 K is graphically represented in Figure 3, 4.

The negative values of the excess thermal expansion coefficient α^E for the examined systems, that become more negative with increasing temperature, indicate that the mixture is more stable than the pure components, which is consistent with the data of the excess molar volume. The observed trend of isothermal coefficient of pressure excess molar enthalpy $(\partial H_m^E/\partial P)_{T,x}$is the opposite of the observed trend for the excess thermal expansion coefficient α^E values. Positive values of $(\partial H_m^E/\partial P)_{T,x}$indicate that by increasing the pressure, the molecular gravity of the system increases in the system under study. This trend is in accordance with equation (9), why so the sign of equation $(\partial H_m^E/\partial P)_{T,x}$ for a mixture, whose volume at constant temperature and constant composition decreases with increasing pressure, should be positive. In other words, the positive values of this quantity indicate that the increase in pressure increases the excess molar enthalpy and the relative instability of the binary system.

3.2 Ternary mixtures

Empirical studies of thermodynamic systems require a lot of time and cost, and with increasing number of components in the study system, these techniques are more difficult and require more time and cost. Therefore, the extraction of the thermodynamic properties of multi-component systems seems to be very beneficial using the thermodynamic data of binary systems.

In this work, the excess molar volumes of ternary mixture of 2-Propanol (1) + 1, 3-Diaminopropane (2) + 2, 5-Dimethoxytetrahydrofuran(3) were calculated using equation (1) and refractive index deviations were calculated using equation (2) and the results were listed in Table 5 and graphically represented in Figure5. Ternary data were fitted to the Cibulka [8], Singh [9], Jasinski and Malanowski [10], Calvo [10], and Nagata [11] equations. These expressions include three terms corresponding to binary contributions evaluated by the Redlich-Kister [6, 7] equation adjusted to the binary data. The expression suggested by:

Cibulka equation:

$$(10)\quad Y^E_{123} = Y^E_{m,binary} + x_1x_2x_3(B_0 + B_1x_1 + B_2x_2)$$

Singh et al. equation:

$$(11)\quad Y^E_{123} = Y^E_{m,binary} + x_1x_2x_3(B_0 + B_1x_1(x_2 - x_3) + B_2{x_1}^2(x_2 - x_3)^2)$$

Jasinski and Malonowski equation:

$$(12)\quad Y^E_{123} = Y^E_{m,binary} + x_1x_2x_3(B_0 + B_1(2x_1 - 1) + B_2(2x_1 - 1)^2)$$

Calvo et al. equation:

$$(13)\quad Y^E_{123} = Y^E_{m,binary} + x_1x_2x_3(B_0 + B_1(2x_1 + 2x_2 - 1) + B_2(2x_1 + 2x_2 - 1)^2$$

Nagata Equation:

$$(14)\quad Y^E_{123} = Y^E_{m,binary} + x_1x_2x_3B$$

where $Y^E_{m,binary}$ are the contributions of binary mixture i, j.

$$(15)\quad Y^E_{m,binary} = Y^E_{12} + Y^E_{13} + Y^E_{23}$$

every B_i ternary parameter is a function of temperature as expressed in Eq. (10)– (14):

$$(16)\quad B_i = \sum_{j=0}^{2} C_{iq}T^q,$$

The parameters C_{iq} for the ternary mixtures are listed in Table 6, along with the standard deviationσ.

3.3 Prediction of Excess Molar Volumes for the Ternary Mixture

Obviously, the thermodynamic properties of ternary systems are strongly dependent on intermolecular interactions of compounds, and it is not easy to predict the thermodynamic properties of these mixtures. In recent years, however, several empirical and semi-experimental equations have been presented in the form of symmetric models for predicting thermodynamic properties. Symmetric models are those geometric models that consider the interactions of ternary systems from the same combination of binary interactions. In order to use these equations, the relationship between the binary systems corresponding to the ternary system must be determined. The Redlich-Kister equation is the most well-known relation in this field. By having the coefficients in these equations and correlating with the empirical results obtained in the laboratory and using the relationship obtained from the Redlich-

Kister equation, excess molar volume is predicted as one of the most widely used thermodynamic properties.

Accordingly, excess molar volumes and refractive index deviations for studied ternary mixtures were predicted using Radojkovic[14], Colinet [15], Jacob-Fitzner [16], Kohler [17], and Rastogi [18] geometrical solution models. These models also use binary contributions evaluated by Redlich–Kister equation and proposed an equation for ternary system of the form:

Radojkovic Model:

$$(17) \qquad Y^E_{123} = Y^E_{12} + Y^E_{13} + Y^E_{23}$$

Colinet Model:

$$(18) \qquad Y^E_{123} = 0.5(Y^E_{12}(x_2/1-x_1) + Y^E_{12}(x_1/1-x_2) + Y^E_{13}(x_3/1-x_1) + Y^E_{13}(x_1/1-x_3) + Y^E_{23}(x_3/1-x_2) + Y^E_{23}(x_2/1-x_3))$$

Jacob-Fitzner Model:

$$(19) \quad Y^E_{123} = {}^{Y^E_{12}x_1x_2}/_{[(x_1+{}^{x_3}/_2)(x_2+{}^{x_3}/_2)]} + {}^{Y^E_{13}x_1x_3}/_{[(x_1+{}^{x_2}/_2)(x_3+{}^{x_2}/_2)]} + {}^{Y^E_{23}x_1x_3}/_{[(x_2+{}^{x_1}/_2)(x_3+{}^{x_1}/_2)]}$$

Kohler Model:

$$(20) \qquad Y^E_{123} = Y^E_{12}(x_1+x_2)^2 + Y^E_{13}(x_1+x_3)^2 + Y^E_{23}(x_2+x_3)^2$$

Rastogi Model:

$$(21) \quad Y^E_{123} = \begin{bmatrix} Y^E_{12}(x_1+x_2) + Y^E_{13}(x_1+x_3) \\ +Y^E_{23}(x_2+x_3) \end{bmatrix} / 2$$

Standard deviation for the fitting of excess molar volumes and refractive index deviations prediction models for ternary mixture (2-ropanol (1) +1, 3-Diaminopropane (2) +2, 5-Dimethoxytetrahydrofuran (3)) using prediction solution model equations (17) - (21) at T = (298.15 to 328.15) K are reported in Table 7. As can be seen in Table 7, in general the agreement between Colinet geometrical solution models is in better consistency with experimental results for both excess molar volumes and refractive index deviations.

4. Conclusion

Understanding of molecular interactions is essential in chemical processes and thermodynamic properties are one of the best means to interpret and justify these interactions. In this paper we obtain densities and refractive indices of binary and ternary mixtures including of 2, 5-Dimethoxytetrahydrofuran, 1, 3-Diaminopropane, and 2-Propanol and its derivatives were obtained from experimental results and fitted by Redlich–Kister type function to obtain the binary coefficients and estimate the standard deviations. V^E_m,Δn_D,α^E and $(\partial H^E_m/\partial P)_{T,x}$ were calculated. By using excess molar volume and refractive index deviations of binary systems from ideal state, molecular interactions are estimated. In general it can be concluded that chemical interactions consequences to negative deviations and the positive quantities are indicated the physical interactions in binary systems.

Acknowledgement

The author would like to thank the Bu-Ali-Sina University for providing the necessary facilities to carry out the research.

References

[1] Duve. G, Fuchs. O, Overbeck. H, Hoechst Solvents: Manual for Laboratory and Industry, 5th ed, Hoechst Aktiengesellschaft, 1974.

[2] Poling. B.E, Prausnitz. J.M, Ó Connel. J.P, The Properties of Gas and Liquid, 5th ed, McGraw-Hill, New York, 2000.

[3] Iloukhani. H. Jafarnejad. M. J, Chem. Thermodyn. 2016, 96, 210.

[4] Khanlarzadeh. K, Iloukhani. H, Soleimani. M. J, Mol. Struct. 2017, 1139, 78.
[5] Jafarnejad. M, Iloukhani. H, Thermochim. Acta. 2016, 639, 160.
[6] Redlich. O, Kister. A.T, Ind. Eng. Chem. 1948, 40, 345.
[7] Marquardt. D, SIAM. J, Appl. Math. 1963, 11, 431.
[8] Cibulka. Y, Collect Czech. Commun. 1982, 47, 1414.
[9] Singh. P.P, Nigam. R. K, Sharma. S. P, Aggarwal. S, Fluid Phase Equilib. 1984, 18, 333.
[10] Domiınguez. M, Gascon. I, Valen. A, Royo. F.M, Urieta. J.S, J.Chem. Thermodyn. 2000, 32, 1551.
[11] Nagata. Y, Tamura. K, J. Chem. Eng. Data. 1988, 33, 283.
[12] Hammett. L.P, J. Am. Chem. Soc. 1937, 59, 96.
[13] Smith. J.W, Parai. S, Basicity and complex formation, John Wiley & Sons Ltd, 1968.
[14] Radojkovic. N, Tasic. A, Grozdanic. D, Djorjevic, B, Malic. M. J, Chem.Thermodyn. 1977, 9, 349.
[15] Colinet. C, Ph.D. Thesis, University of Grenoble, France, 1967.
[16] Jacob. K.T, Fitzner. K, Thermochim. Acta. 1977, 18, 197.
[17] Kohler. F, Monatsh. Chem. 1960, 91, 738.
[18] Rastogi. R.P, Nath. J, Das. S.S, J. Chem. Eng. Data, 1977, 22, 249.
[19] Pang. F.M, Senga. C.E, Teng. T. T, Ibrahim. M.H, J. Mol. Liq. 2007, 136, 71.
[20] Iloukhani. H, Almasi. M, Thermochim. Acta, 2009, 495, 139.
[21] González. E.J, González. B, Calvar. N, Domínguez. A, J. Chem. Eng. Data, 2007, 52, 1641.
[22] Weast. R.C, CRC Handbook of Chemistry and Physics, 58th Ed. CRC, 1978.
[23] Kimura. T, Ozaki. T, Nakai. Y, Takeda. K, Takagi. S, J. Therm. Anal. 1998, 54, 285.
[24] Kimura. T, Kitai. T, Kamiyama. T, Fujisawa. M, Thermochim. Acta. 2006, 450, 91.
[25] Saleh. M.A, Ahmed. M.S, Islam. M.S, Phys. Chem. Liq. 2002, 40, 477.

Communications In Catalysis
Vol. 1, No. 2, 2018, pp.65-70
DOI: 10.22049/CIC.2018.26369.1025

Azarbaijan Shahid Madani University

Application of Carbon Nano Tubes for Fabricate Nano Capacitor Including Boron Nitride Dielectric

Nabieh Farhami, Majid Monajjemi[b*], Karim Zare[c]

[a,b,c] Chemistry Department, Faculty of Science, Science and Research Branch, Islamic Azad University, Tehran, Iran

*Corresponding author. Tel.: +98 (913) 8663405; Fax: +98 (313) 7811321

E-mail address: m_monajjemi@yahoo.com

Received: 2025-02-02, Revised: 2025-02-20, Accepted: 2025-02-30

Abstract

In this work Nano capacitor was studied by carbon nanotubes electrodes and dielectric of nanotube Boron Nitride. In this research, there are four different configurations which consists of (3,3) & (6,6) & (13,13), (4,4) & (8,8) & (14,14), (5,5) & (10,10) & (15,15), (6,6) & (12,12) & (17,17) and also we calculated total charge electric, potential difference between electrodes, capacity and dielectric constant. All calculations are based on DFT theory and semi empirical method.

Keywords: Boron Nitride nanotube, Capacitor, Carbon nanotube, quantum mechanics

Introduction

Fuel cells, batteries and capacities are systems that are widely used to store energy. Conventional capacitors and batteries have limitations, including short response time. This is due to the movement towards ions in the electrochemical reaction. Recent advances in Nano-scale physics have increased our understanding of the mechanism of energy storage in Nano-materials. Besides reversibility, the effect and high capacity of energy storage and low weight nanostructures, have been considered. Nano structure capacitors have high energy density and are able to store and release the large amounts of lead at speed. Nano capacitors have high to load to transfer rates, long life and short cycle charge compared to batteries which make them useful for a variety of applications [1-4]. Because their nanometer size and their properties such as electrical conductivity, mechanical strength available surface, low resistance and high stability carbon nanotubes are suitable as capacitor electrodes [5]. There are two types of carbon nanotube electrodes 1- bind free [6] 2- binder-enriched [7]. The mentioned types of electrodes are used in electrochemical capacitors [8]. After the discovery of carbon nanotubes in 1991[9], Boron Nitride nanotubes (BNNTs) were synthesized in 1995. There exists sp^2 bonds that cause the strength of these tubes. The predicted elastic modulus for this material is approximately 850 GPa [9]. In some features Boron Nitride nanotubes are better than carbon nanotubes. Theoretical studies have predicted that nanotube Boron Nitride is an insulating material. Its electrical energy gap is about 5/5 eV [10]. These characteristics do not depend on the diameter and chirality of the nanotubes based on conductivity measurements all BNNTs exhibit insulating or semi conducting behavior. Also, BNNTs have more stable chemical properties. For example, they have higher resistance to oxidation at high temperature up to 800^0C. Some of BNNTs that have the complete Nano-crystalline structures can have a thermal resistance of up to 900^0 C. This is while carbon nanotubes are easily in the air at 400^0 C and burn completely at 700^0 C [11]. BNNTs have three different types of configurations, 1-zigzag (n, 0) 2-arm chair (n, n) 3- non chiral (n, m). Depending on the synthesis methods, different configurations of the nanotubes are generated [13-17].

Details of calculation

Figure 1 shows the cross section of a cylindrical capacitor of length l, which consists of two coaxial cylinders in radius (a) and (b) with q charge on each tube. Since $l \gg b$, it is possible to ignore of non -uniformity of the edges.

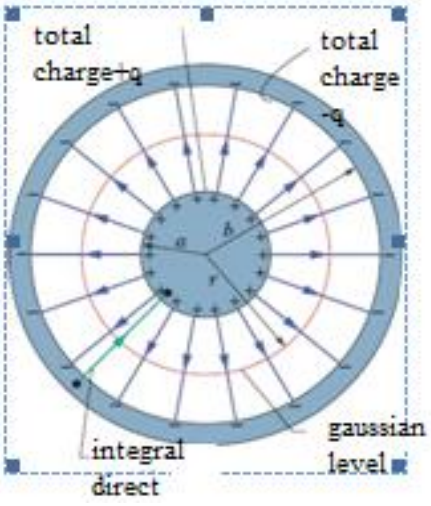

Fig1. Cross section of a cylindrical capacitor

The Gaussian level is selected as a cylinder of length l and radius r and axially with cylinder which includes a central cylinder. There for, the Gaussian level contains the charge in following equation 1.

(1) $q = \varepsilon EA = \varepsilon E\left(2\pi rl\right)$

'A' is the area of the cross section of the Gaussian side and the flow doesn't pass from the surface of the two cylinders. By solving the above equation, we will have an electric field, equation 2:

(2) $E = \frac{q}{2\pi rl\,\varepsilon}$

In the eq 2, $\varepsilon = \kappa\varepsilon_0$, ε_0 is the value of the permittivity for air which is $8/85*10^{-12}$ f/m and K is the permittivity of the dielectric medium used between the two tubes. Also The potential is obtained by the integral, it is as follows 3:

(3) $V = \int_{-}^{+} Eds = \frac{-q}{2\pi\varepsilon l}\int_{b}^{a}\frac{dr}{r} = \frac{q\ln\left(\frac{b}{a}\right)}{2\pi\varepsilon l}$

dr =ds. By using of the relation c=q/v, capacity is obtained by equation 4:

(4) $c = \frac{2\pi\varepsilon l}{\ln\left(\frac{b}{a}\right)}$

Theorical model

In this work, the calculations were carried on model. In this model a small capacitor was made by creating an insulating tube of BN between two carbon tubes, for making this model nanotube modeler software was used, figure 2.

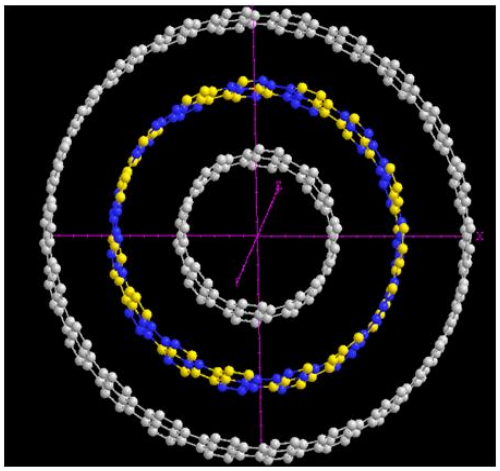

Fig2. Model of Nano capacitor

The calculations were performed by using Gaussian 09 software and the method of DFT and semi empirical method and chelpg and extended Huckel commands and m06-2x. The m06-L, m06-2x and m06-HF are new method hybrid DFT functional method with a good correspondence in non -bonded calculations are useful for calculating the energies of the distances between two coaxial cylinders of radius R_{in}, R_{out} and in the cylindrical capacitor. The lattice constant has been optimized for the atomic coordinate and has done through the minimization of the total energies. For geometries optimizations, all the internal coordinates were relaxed until the Hellmann- Feynman- forces were less than 0.05 angstrom. At each inter tube configuration, a single point calculation is carried out and the total energies are recorded, the resulting sliding rotation energy surface is used for fixing our model in a better position. We used DFT theories with the van der Waals DFT for modeling the exchange – correlation energies of BNNT and CNT. The DZV(double zeta basis set) basis set with polarization orbital was used for

nanotube. The charge transfer and electrostatic potential were calculated via an extended Huckel method. The extended Huckel is a semi empirical method. For a non -covalent interaction, B3LYP cannot to describe Vander Waals interaction [18-19] in capacitor systems by medium rang interactions, such as the interactions of two electrodes and dielectric sheet. Failure of B3LYP and the other functional to describe medium range of exchange and correlation energy correctly, limits their suitability for non bonded distant systems of two electrodes and dielectric in a capacitor. The most recent studies have shown that in exactitude for the medium range exchange energies lead to large systematic errors in the divination of molecular properties [20-24].

Results and discussion

In this studying, BNNT, was chosen as a dielectric because it is an excellent spacer with a lattice constant close to the carbon nanotube (CNT). We specially studied the dielectric properties of CNT/ BNNT/ CNT, the sp^2 hybridized B-N and C-C bonding has the similar properties in mechanics, but their optic and electronic properties are different. Fundamentally the equivalent points result from the close positions of N, B and C in the Mendeleev table, but the different ones result from the heterogeneous atoms. The bonding orbit p of B-N is principally dominated by 2p orbit of N and 2p orbit of B contributes mostly to the anti-bonding orbit p*.

It was considered that the electrodes carry ±q charges from one electrode towards the opposite side. So the initial energy stored in the electrical field between the capacitor tubes is obtained by $E_i=q^2/2c$, one of the fundamental effects in Nano electronics are related to the significant change in the energy when the electrons are transferred into a Nano material such as quantum dot. By letting the electrons tunnel through the insulating tube from the negative terminal to the positive terminal and stored energy is $E_f = (q+\Delta q)^2/2c$. Although the charge is quantized itself, but the charge on the capacitor tubes is polarized and not quantized. The energy cannot stored in the capacitor tubes until a single electron tunnels through the insulator BN tubes from the negative terminal to the positive terminal that energy is $\Delta E= E_f - E_i$, when the quantum well descends below the Fermi level, the electrons start to pour in this quantum well and the excess electrons in the carbon nanotubes become sensitive to charge reveal into the vacuum space of capacitor.

In the Table 1 four different configurations and their diameter are shown. d_1 is diameter of internal carbon nanotube, d_2 is diameter of BNNT and d_3 is diameter of external carbon. The values of the electric charge from $(\left|\Delta q \times 10^{20}\right|)c = \sum q_{out} - q_{in}$ are shown in the table2. Electric charge has Coulomb(c) unit. The potential difference is obtained from equation $\Delta V = \sum (V_{out} - V_{in})$

V_{out} is average potential difference of external electrode and V_{in} is average potential difference of internal electrode, Table2. The q_{out}, q_{in}, V_{out} and V_{in} were obtained from Gaussian program computations.

The following equation is used to calculate the capacity c=q/v, capacity has farad unit,

table2. K is calculated by equation 4. The values of K are obtained 5/9 for total configurations.

Conclusion

We studied Four different configurations consists of (3,3) & (6,6) & (13,13), (4,4) & (8,8) & (14,14), (5,5) & (10,10) & (15,15), (6,6) & (12,12) & (17,17). Total charge electric, potential difference between electrodes, capacity and dielectric constant were calculated, Table 2.

BNNT usually can be used as an insulator regardless of its diameter and helicity or the number of walls and dielectric constant of Boron Nitride nanotubes doesn't depend on diameter and configuration. Capacity for four different configurations increased from the increase diameters. These Nano capacitors were sensitive to the existence of molecules inside them and are under the influence of the resulting induced electrostatic field. The structural properties of these Nano capacitors had the ability of transferring charges and electromagnetic current to bonds and the charge transfer along the Nano capacitors, created a regular electromagnetic current around the Nano capacitors. These quantity values exhibited a Gaussian distribution and different expectation values could be referred to each quantized level. It seems that research on such a non -bonded interaction in the carbon Nano tube would be a promising way to cure the chemical and physical properties of carbon compounds and may avail as a starting point for designing electromagnetic Nano systems to be considered in experiments.

Acknowledgments

Hereby, the first author acknowledges the Science and Research branch of Islamic Azad University of Tehran and Islamic Azad University, Mahshahr branch, for supporting us to prorate software and computational instrument in informatics lab.

Table1. Four different configurations and their diameter

Nano capacitor CNT/BNNT/CNT	$d_1 *10^{10}$(m)	d_2*10^{10} (m)	$d_3 *10^{10}$ (m)
(3,3)@(6,6)@(13,13)	4/039	8/079	17/504
(4,4)@(8,8)@(14,14)	5/38	10/77	18/85
(5,5)@(10,10)@(15,15)	6/73	13/46	20/197
(6,6)@(12,12)@(17,17)	8/079	16/157	22/89

Table2. The total charge, potential difference and capacity values calculated for different configurations

Nano capacitor CNT/BNNT/CNT	$(\lvert\Delta q\times 10^{20}\rvert)c=\sum q_{out}-q_{in}$	$(\Delta V)v=\sum V_{out}-V_{in}$	$(c\times 10^{20})f$
(3,3)@(6,6)@(13,13)	1/2675	0/039	32/68
(4,4)@(8,8)@(14,14)	1/3142	0/034	38/35
(5,5)@(10,10)@(15,15)	1/5765	0/036	43/68
(6,6)@(12,12)@(17,17)	1/136	0/025	46/13

References

[1] Winter. M, Brodd. R.J, J. Chem. Rev. 2004, 104, 4245-4270.

[2] Pandolfo. A.G, Hollen Kamp. A.F, J. pow. Sou. 2006, 157, 11-27.

[3] Yildirim. T, Ciraci. S, Phy. Rev. Lett. 2005, 94, 175501.

[4] Durgun. E, Ciraci. S, Yildirim. T. Phy. Rev.Lett. 2006, 97, 226102.

[5] Zhang. L.L, Zhou. R, Zhao. X.S, J. Mat. Chem. 2010, 20, 5983-5992.

[6] Niu. C, Sichel. E. K, Hoch. R, Moy. D,Tennent. H. Appl. Phy. Lett. 1997, 70, 1480.

[7] Ma. R, Liang. J, Wei. B, Zhang. B, Xu. C, Wu. D, Bull. Chem. Soc. Jap. 1999, 72, 2563.

[8] Ma. J, tang, J, Zhang. H, Shinga. N, Qin. L.C, ACS Nano. 2009, 3, 3679-3683.

[9] Weihong. T.O, phys. Rev. lett. 2011, 106, 236805.

[10] Balzer. B, Kyung. D, S´en´echal. A. M. S, Tremblay. M, Potthoff, Euro. Phy. Lett. 2009, 85, 1700.

[11] Blasé. X, Rubio. A, Louie. S.G,Cohen. M.L, Phys. Rev B. 1995, 51, 6868.

[12] Chen. H, Advan. Mat. 2007, 19, 1845, 2007.

[13] Smith. M. W, Jordan. K. C, Park. C, Kim. J, Lillehei. P. T, Crooks. R, Harrison. J.S, 2009, 20, 505604.

[14] Chen. Y, Nano. 2008, 2, 367.

[15] Lee. C. H, Qin. S, Savaikar. M. A, Wang. J, Hao. B, Zhang. D, Banyai. D, Jaszczak. J. A, Clark. K. W, Idrobo. J. C, Li. A. P, Yap. Y. K, Advan. Mat. 2013, 25, 4544.

[16] Yu. J, Advan. Mat, 2006, 18, 2157.

[17] Ciofani. G, Danti. S, Genchi. G.G, Mazzolai. B, Mattoli. V, Small, 2013, 9, 1672–1685.

[18] Monajjemi. M, Chem. Phy, 2013, 425, 29.

[19] Monajjemi. M, Heshmat. M. Aghaei. H, Ahmadi. R, Zare. K, Bull. Chem. Soc. Ethi. 2007, 21, 1.

[20] Monajjemi. M, Honarparvar. B. H, Haeri. H, Heshmat. M, Russ. J. Phys. Chem. 2006, 80, 40.

[21] Monajjemi. M, Ketabi. S, Amiri. A, Russ. J. Phys. Chem. 2006, 80, 55.

[22] Yahyaei. H. Monajjemi. M, Aghaei. H, Zare. K. J, Compu. Theor. Nano Sci. 2013, 10, 2332.

[23] Zawari. M, Haghighizadeh, M, Derakhshandeh. M, Barmaki. Z, Farhami. N, Monajjemi. M. J, Comput. Theo. Nano. Sci. 2015, 12, 5472.

[24] Farhami. N, Monajjemi. M, Zare. K, Orient. Chem. 2017, 33, 3024.